Thermal boundary layer structure in low-Prandtl-number turbulent convection

Ambrish Pandey†

Center for Space Science, New York University Abu Dhabi, PO Box 129188 Abu Dhabi, UAE

We study the structure of the thermal boundary layer (BL) in Rayleigh–Bénard convection for Prandtl number (Pr) 0.021 by conducting direct numerical simulations in a two-dimensional square box for Rayleigh numbers (Ra) up to 10^9. The large-scale circulation in the flow divides the horizontal plates into three distinct regions, and we observe that the local thermal BL thicknesses in the plume-ejection region are larger than those in the plume-impact and shear-dominated regions. Moreover, the local BL width decreases as $Ra^{-\beta(x)}$, with $\beta(x)$ depending on the position at the plate. We find that the values of $\beta(x)$ are nearly the same in the impact and shear regions, and are larger in the ejection region. Thus, the local BL width decreases faster in the ejection region than in the shear and impact regions, and we estimate that the thermal BL structure would be uniform throughout the horizontal plate for $Ra \geq 8 \times 10^{12}$ in our low-Pr convection. We compare the thermal BL profiles measured at various positions at the plate with the Prandtl–Blasius–Pohlhausen (PBP) profile and find deviations everywhere for all the Rayleigh numbers. However, the dynamically rescaled profiles, as suggested by Zhou & Xia (*Phys. Rev. Lett.*, vol. 104, 2010, 104301), agree well with the PBP profile in the shear and impact regions for all the Rayleigh numbers, whereas they still deviate in the ejection region. We also find that, despite the growing fluctuations with increasing Ra, thermal boundary layers in our low-Pr convection are transitional and not yet fully turbulent.

Key words: boundary layer structure, Bénard convection, turbulent convection

---

1. Introduction

Turbulent flows driven by thermal convection occur commonly in nature. For example, the flows in the convection zone of the Sun and the Earth's outer core are driven primarily by the buoyancy force arising due to the inhomogeneous temperature field (Hanasoge, Gizon & Sreenivasan 2016; Pandey, Scheel & Schumacher 2018*a*; Schumacher & Sreenivasan 2020). The Prandtl number (Pr), which is the ratio of the kinematic viscosity ν and the thermal diffusivity κ of a fluid, is approximately 10^{-6} in the solar convection zone (Schumacher & Sreenivasan 2020) and $Pr \approx 10^{-2}$ in the Earth's outer core (Schumacher, Götzfried & Scheel 2015). Rayleigh–Bénard convection (RBC) is a paradigm of turbulent convection flows in nature, where a fluid kept between two horizontal plates is heated from below and cooled from above (Ahlers, Grossmann & Lohse 2009; Chillà & Schumacher 2012; Verma, Kumar & Pandey 2017; Verma 2018).

† Email address for correspondence: ambrish.pandey@nyu.edu

The main governing parameters of RBC are the Prandtl and Rayleigh numbers, where the Rayleigh number *Ra* indicates the strength of the thermal driving force compared to the viscous dissipative forces in the flow. Thin viscous and thermal boundary layers (BLs) near the isothermal horizontal plates exist in RBC, and the behaviour of the flow in the BL region remains laminar-like even up to very large *Ra* despite a highly turbulent flow in the bulk region away from the walls. Properties of low-*Pr* convection flows differ in certain aspects from those of high-*Pr* flows. In low-*Pr* RBC, the thermal BL is thicker compared to the viscous BL, and therefore directly interacts with the turbulent bulk flow. Moreover, low-*Pr* RBC is dominated by the inertial effects and is highly turbulent compared to high-*Pr* convection flows at the same *Ra* (Schumacher *et al.* 2015; Pandey & Verma 2016; Scheel & Schumacher 2017; Shishkina *et al.* 2017; Pandey *et al.* 2018*a*). The structure of the thermal BL has primarily been explored for moderate- (Shi, Emran & Schumacher 2012; Wagner, Shishkina & Wagner 2012; Scheel & Schumacher 2014) and high-*Pr* RBC (Werne 1993; Lui & Xia 1998; Wang & Xia 2003; Zhou *et al.* 2011), where the thermal BL is either of a similar width to the viscous BL or nested within the latter. In this paper, we study the horizontal structure of the thermal BL in a low-*Pr* RBC.

Characterization of the thermal BL is important as it controls the global heat transport, which is quantified using the Nusselt number (*Nu*) (Grossmann & Lohse 2000). In RBC, the mean thermal BL width can be computed as $H/(2Nu)$ (Ahlers *et al.* 2009; Chillà & Schumacher 2012), and this relation has been verified for a wide range of *Ra* and *Pr* (Stevens, Lohse & Verzicco 2011; Scheel, Kim & White 2012; Zhou & Xia 2013; Scheel & Schumacher 2014, 2016; Schumacher *et al.* 2016; Scheel & Schumacher 2017; Zhang *et al.* 2017*a*; Bhattacharya, Samtaney & Verma 2019). This relation arises from the definition of the thermal BL thickness using the slope method (Wagner *et al.* 2012) and from the fact that the heat transport is purely diffusive at the horizontal plates. The thermal BL thickness, however, is a local quantity and varies in magnitude at the horizontal plates. For high-*Pr* RBC, local BL thickness has been observed to be the smallest near the center of the plate and to increase symmetrically (Lui & Xia 1998) or asymmetrically (Werne 1993; Wang & Xia 2003; Zhou *et al.* 2011) in the plane of the large-scale circulation (LSC) as the sidewalls are approached. For moderate-*Pr* RBC, Wagner *et al.* (2012) observed that the local BL thickness increases almost linearly along the direction of LSC, whereas Scheel & Schumacher (2014) observed that the local BL thicknesses are larger at the plume-detachment locations. In this paper, we find that the local BL thickness in low-*Pr* RBC varies asymmetrically along the plate, and its relative variation in the central region of the plate decreases from around 3.1 at $Ra = 5 \times 10^5$ to around 1.6 at $Ra = 10^9$.

In turbulent RBC, nearly all the imposed temperature difference occurs primarily in the thin thermal BLs, whereas the bulk region remains mostly isothermal. The thermal BL profiles in RBC have been compared with the Prandtl–Blasius–Pohlhausen (PBP) profile, which was originally proposed for a laminar shear flow on a semi-infinite heated plate (Landau & Lifshitz 1987; Shishkina *et al.* 2010), and systematic deviations with increasing *Ra* and decreasing *Pr* have been reported (Shishkina & Thess 2009; Zhou *et al.* 2010, 2011; Shi *et al.* 2012; Stevens *et al.* 2012; Shishkina *et al.* 2015; Ovsyannikov *et al.* 2016; Wang, He & Tong 2016; Shishkina *et al.* 2017; Wang *et al.* 2018). As the Prandtl–Blasius BL theory is based on the two-dimensional (2-D) equations, the BL profiles obtained from 2-D flows are more likely to be closer to the PBP profile. Van der Poel, Stevens & Lohse (2013) compared the thermal BL profiles at the center of the horizontal plate in two- and three-dimensional (3-D) RBC for $Pr = 4.38$ and $Ra \approx 10^8$, and observed that the BL profile in 2-D is indeed closer to the PBP profile compared to that in 3-D. They credited the larger deviation from the PBP profile in 3-D RBC to increased plume

activity compared to that in 2-D RBC. The agreement with the PBP profile has been observed to improve if the profiles are averaged in a dynamical frame of reference based on the instantaneous BL thicknesses (Zhou *et al.* 2010, 2011; Scheel *et al.* 2012; Shi *et al.* 2012; Stevens *et al.* 2012). Nonetheless, persistent deviations even after using this dynamic rescaling have been reported in 3-D RBC for moderate- and high-*Pr* RBC (Scheel *et al.* 2012; Shi *et al.* 2012; Stevens *et al.* 2012). The local thermal BL profiles have not been compared with the PBP profile in low-*Pr* RBC, except for the horizontally-averaged profiles, which exhibit increasing deviation with decreasing *Pr* (Scheel & Schumacher 2016; Shishkina *et al.* 2017; Ching *et al.* 2019). Therefore, we measure the temperature profiles at various horizontal positions in our low-*Pr* RBC and observe deviations from the PBP profile everywhere, with the degree of deviation depending on the measurement position.

As mentioned above, the properties of the near-wall temperature field have mostly been studied in moderate- and high-*Pr* RBC, as the investigations of low-*Pr* convection are inhibited by several experimental and numerical challenges. On the one hand, the opaqueness of low-*Pr* fluids, such as mercury, gallium or liquid sodium, restricts the use of optical measurement techniques (Cioni, Ciliberto & Sommeria 1997; Glazier *et al.* 1999; Zürner *et al.* 2019). On the other hand, numerical investigations of low-*Pr* convection require massive computational resources, as very small length and time scales need to be resolved accurately to prudently study them (Pandey & Verma 2016; Scheel & Schumacher 2016; Schumacher *et al.* 2016; Scheel & Schumacher 2017; Shishkina *et al.* 2017; Pandey *et al.* 2018a). Note that exploring convection in very high-*Pr* fluids also requires significant computational resources, as the smallest length scale in the temperature field, the Batchelor scale η_B, becomes much finer compared to the Kolmogorov length scale η_K, which is the smallest length scale in the velocity field (Silano, Sreenivasan & Verzicco 2010; Horn, Shishkina & Wagner 2013; van der Poel *et al.* 2013; Pandey, Verma & Mishra 2014; Shishkina *et al.* 2015, 2017). These two length scales are related by $\eta_B = \eta_K/\sqrt{Pr}$ (Shishkina *et al.* 2010), and thus, it is the Batchelor scale that needs to be resolved properly to prudently study high-*Pr* convection. Thanks to growing computational resources, properties of the temperature field in the BL region have been explored only recently in low-*Pr* RBC (Scheel & Schumacher 2016; Schumacher *et al.* 2016; Scheel & Schumacher 2017; Shishkina *et al.* 2017).

Scheel & Schumacher (2016) computed the local thermal BL thicknesses in a cylindrical cell of aspect ratio unity for $Pr = 0.005, 0.021, 0.7$ using the local vertical temperature gradient at the horizontal plates and observed that the mean BL thicknesses are larger when the regions near the sidewall are included. They also observed that the horizontally- and temporally-averaged thermal BL profile for the lower Prandtl numbers deviates from the corresponding profile for $Pr = 0.7$. Scheel & Schumacher (2017) computed the displacement thicknesses and shape factors (defined respectively in (5.11) and (5.10) here) of the mean temperature profiles and found that the displacement thicknesses increase with decreasing *Pr* and the shape factors deviate from those of the corresponding PBP profiles. Schumacher *et al.* (2016) and Scheel & Schumacher (2017) compared the mean temperature profiles in low-*Pr* RBC with the fully turbulent BL profile, which exhibits a logarithmic region, and observed that the region where the logarithmic scaling is observed in the profiles increases with increasing *Ra*. Shishkina *et al.* (2017) proposed an analytical form of the mean thermal BL profile by incorporating the effects of turbulent fluctuations in the BL equations, and observed very good agreement with their numerically computed profiles in a cylindrical RBC cell of aspect ratio unity for *Pr* between 0.01 and 2547.9. The detailed horizontal structure of the thermal BL in

low-*Pr* convection is, however, still unexplored and is the primary objective of this paper.

In this work, we conduct direct numerical simulations (DNS) of RBC in a low-*Pr* fluid at high Rayleigh numbers and study the structure of the thermal BL. We simulate convection flows for $Pr = 0.021$, which is a typical Prandtl number for mercury or gallium, and for $Ra = 5 \times 10^5$ to $Ra = 10^9$ in a 2-D square box. Although turbulent flows in nature are 3-D, the characteristics of some of them can be understood using 2-D or quasi-2-D models. For instance, turbulent convective flows under the effects of a strong rotation or a strong magnetic field behave similarly to quasi-2-D flows (Chandrasekhar 1981). In RBC of aspect ratio around unity, the LSC is usually the strongest flow structure, and the BL structure has primarily been explored along the direction of LSC (Lui & Xia 1998; Wang & Xia 2003; Wagner *et al.* 2012). However, the plane of LSC does not remain fixed in 3-D RBC, which poses an additional challenge in the study of the BL structure as one has to be in the direction of LSC at every instant. Furthermore, we choose a 2-D geometry as (i) almost all the BL theories have been developed for 2-D flows; (ii) the measurement probes always remain in the plane of LSC, in contrast to RBC in a cylindrical cell, where the plane of LSC exhibits reorientation (Wagner *et al.* 2012; Schumacher *et al.* 2016; Zürner *et al.* 2019); and (iii) high Rayleigh numbers can be achieved even with moderate computational resources; the highest *Ra* explored in this work has not been achieved in 3-D DNS at this *Pr* (Scheel & Schumacher 2017). Note that 2-D RBC has been utilized to better understand some of the important phenomena in convection, e.g. the properties of flow reversals (Sugiyama *et al.* 2010; Chandra & Verma 2013; Podvin & Sergent 2015; Pandey, Verma & Barma 2018*b*; Zhang *et al.* 2020), the onset of the ultimate regime of convection (Zhu *et al.* 2018), and the logarithmic temperature profiles (van der Poel *et al.* 2015; Zhu *et al.* 2018). We detect LSC in our simulations, which yields three different regions, namely, the plume-ejection, shear-dominated and plume-impact regions, at the horizontal plates (van der Poel *et al.* 2015; Schumacher *et al.* 2016; Zhu *et al.* 2018). Using our DNS data, we explore the horizontal dependence of the local thermal BL thickness and find that the local thicknesses in the ejection region are larger than those in the shear and impact regions. We measure the temperature profiles in the aforementioned regions and observe that they deviate from the PBP profile for all *Ra*. However, once the profiles in the shear and impact regions are dynamically rescaled (Zhou & Xia 2010), they agree very well with the PBP profile. We also find that due to growing turbulent fluctuations with increasing *Ra*, the local temperature profiles in the ejection region become increasingly similar to the fully turbulent thermal BL profile. However, the explored Rayleigh numbers are still not large enough to yield a fully turbulent thermal BL.

2. Details of direct numerical simulations

Conservation of momentum, internal energy and mass lead to equations that govern the dynamics of RBC (Chillà & Schumacher 2012; Verma *et al.* 2017; Verma 2018). The non-dimensional governing equations under the Oberbeck–Boussinesq approximations are

$$\frac{\partial \boldsymbol{u}}{\partial t} + \boldsymbol{u} \cdot \nabla \boldsymbol{u} = -\nabla p + T\hat{z} + \sqrt{\frac{Pr}{Ra}} \nabla^2 \boldsymbol{u}, \tag{2.1}$$

$$\frac{\partial T}{\partial t} + \boldsymbol{u} \cdot \nabla T = \frac{1}{\sqrt{RaPr}} \nabla^2 T, \tag{2.2}$$

$$\nabla \cdot \boldsymbol{u} = 0, \tag{2.3}$$

Run	Ra	N_e	N	N_{bl}	$Nu \pm \Delta Nu$	Nu_{ε_T}	Nu_{ε_u}	$Re \pm \Delta Re$	$\dfrac{\Delta_{max}}{\eta_K}$	t_{total} (t_f)	N_s
1	5×10^5	5184	7	180	5.2 ± 0.01	5.2	5.2	6012 ± 1	2.8	121	575
1a	5×10^5	52 900	3	100	5.2 ± 0.01	5.2	5.2	6011 ± 1	0.58	114	125
2	10^6	5184	7	170	6.3 ± 0.05	6.3	6.3	6806 ± 13	3.5	111	400
2a	10^6	52 900	3	90	6.3 ± 0.01	6.3	6.3	6775 ± 82	0.74	133	250
3	10^7	52 900	9	210	10.8 ± 0.01	10.8	10.7	$22\,473 \pm 410$	0.56	101	340
3a	10^7	52 900	5	120	11.1 ± 0.5	11.1	11.0	$22\,187 \pm 110$	0.98	132	400
4	10^8	52 900	11	215	19.6 ± 0.1	19.7	19.3	$97\,118 \pm 1566$	0.97	97	590
5	10^9	198 916	13	360	35.4 ± 1.6	36.6	33.9	$432\,930 \pm 191$	0.85	8.6	452
5a	10^9	198 916	7	190	36.2 ± 0.1	37.4	34.7	$433\,305 \pm 420$	1.5	14.4	717

TABLE 1. Important parameters of our DNS runs at a fixed $Pr = 0.021$ in a 2-D unit square box. Here, N_e is the total number of spectral elements in the flow domain; N is the order of Legendre interpolation polynomials within each element; N_{bl} is the number of grid points within each thermal BL; Nu, Nu_{ε_T} and Nu_{ε_u} are the globally- and temporally-averaged Nusselt numbers computed using (2.5), (2.7) and (2.6), respectively; Re is the Reynolds number computed using the root-mean-square (rms) velocity; Δ_{max}/η_K is the ratio of the maximum grid spacing to the Kolmogorov length scale in the flow; t_{total} is the total integration time after reaching the statistically steady state in units of the free-fall time t_f; and N_s is total number of equidistant snapshots stored for the duration t_{total} and used for the analyses in this paper. The error bars in Nu and Re indicate the differences between the mean values computed over the first and second halves of the datasets.

where $\boldsymbol{u} = (u_x, u_z)$, T and p are respectively the velocity, temperature and pressure fields defined on a 2-D bounded domain. The above equations are non-dimensionalized using H, ΔT, u_f and t_f as the length, temperature, velocity and time scales, respectively, where $u_f = \sqrt{\alpha g \Delta T H}$ is the free-fall velocity and $t_f = H/u_f$ is the free-fall time. The Rayleigh number is defined as $Ra = \alpha g \Delta T H^3 / \nu \kappa$, where α is the thermal expansion coefficient of the working fluid, g is the acceleration due to gravity, and ΔT is the temperature difference between the top and bottom plates separated by distance H.

We perform DNS in a 2-D square box of length $L = H = 1$ by integrating (2.1)–(2.3). We employ the no-slip condition for the velocity field on all the boundaries. The horizontal plates are isothermal and the sidewalls are adiabatic. We use a spectral element solver NEK5000 (Fischer 1997; Scheel, Emran & Schumacher 2013) to simulate the RBC flow for $Pr = 0.021$ for $Ra = 5 \times 10^5$ to $Ra = 10^9$. The flow domain is divided into N_e spectral elements, and the turbulence fields are expanded within each element using Nth-order Legendre polynomials. Thus, we probe our flow domain with $N_e N^2$ mesh cells. We use a denser grid near all the boundaries to capture the strong variations of the velocity and temperature fields in the BLs. The important parameters of our simulations are summarized in table 1.

We start our simulations from the conduction state with random perturbations and wait until a statistically steady state is reached, i.e. when the time-averaged values of the global quantities, such as the convective heat flux and total kinetic energy, do not change significantly. For instance, we separately compute Nu and Re for the first and second halves of the datasets and denote the difference between the mean values over the two halves as ΔNu and ΔRe, respectively (Scheel & Schumacher 2014, 2016). In table 1, we list ΔNu and ΔRe as the error bars in Nu and Re, which show that the mean values

of the global quantities in our simulations do not vary by more than 5 % in the steady state. Due to a larger time scale for the momentum diffusion compared to that for the heat diffusion, the smallest structures in the velocity field in low-*Pr* convection are much finer than the smallest structures in the temperature field (Pandey & Verma 2016; Scheel & Schumacher 2016). Therefore, it is crucial to adequately resolve very fine spatial and temporal Kolmogorov scales in low-*Pr* RBC. The Kolmogorov length scale is computed as $\eta_K = (\nu^3/\varepsilon_u)^{1/4}$, where ε_u is the viscous dissipation rate, defined by

$$\varepsilon_u(\boldsymbol{x}) = \frac{\nu}{2}\left(\frac{\partial u_i}{\partial x_j} + \frac{\partial u_j}{\partial x_i}\right)^2. \tag{2.4}$$

Here, u_i is the component of the velocity in the x_i-direction. For a well-resolved simulation, the maximum grid spacing Δ_{max} in the entire flow domain should be smaller than or comparable to η_K and η_B. The Batchelor scale in our low-*Pr* flow is coarser than the Kolmogorov scale. Therefore, we estimate the Kolmogorov scale using the globally- and temporally-averaged viscous dissipation rate and list the ratio Δ_{max}/η_K in table 1. We can see that for most of our simulations Δ_{max}/η_K is smaller than one, which indicates that the smallest length scales in our flow are resolved adequately.

An important quantity in RBC is the Nusselt number, which is defined as the ratio of the total heat transport to that occurring through conduction alone (Ahlers *et al.* 2009; Chillà & Schumacher 2012; Verma 2018). The globally- and temporally-averaged Nusselt number in our non-dimensional units is computed as

$$Nu = 1 + \sqrt{RaPr}\langle u_z T\rangle_{A,t}, \tag{2.5}$$

where $\langle\cdot\rangle_{A,t}$ denotes the average over the entire simulation domain and the integration time. The Nusselt number can also be computed using the exact relations in RBC, as follows (Shraiman & Siggia 1990; Zhang, Zhou & Sun 2017*b*):

$$Nu_{\varepsilon_u} = 1 + \frac{H^4}{\nu^3}\frac{Pr^2}{Ra}\langle\varepsilon_u\rangle_{A,t}, \tag{2.6}$$

$$Nu_{\varepsilon_T} = \frac{H^2}{\kappa(\Delta T)^2}\langle\varepsilon_T\rangle_{A,t}. \tag{2.7}$$

Here ε_T is the thermal dissipation rate, defined as the rate of loss of thermal energy per unit mass, and computed as

$$\varepsilon_T(\boldsymbol{x}) = \kappa\left[\left(\frac{\partial T}{\partial x}\right)^2 + \left(\frac{\partial T}{\partial z}\right)^2\right]. \tag{2.8}$$

The requirement of resolving very fine Kolmogorov scales significantly increases the computational effort needed to explore convection at low Prandtl numbers (van der Poel *et al.* 2013; Schumacher *et al.* 2015; Pandey & Verma 2016; Scheel & Schumacher 2016; Schumacher *et al.* 2016; Scheel & Schumacher 2017; Pandey *et al.* 2018*a*; Zwirner *et al.* 2020). Due to inadequate spatial resolution, the velocity and temperature derivatives, and, in turn, the viscous and thermal dissipation rates, are inaccurately estimated. In our spectral element simulations, this inadequacy of spatial resolution is reflected in the vertical profiles of the dissipation rates, which do not vary smoothly at the element boundaries (Scheel *et al.* 2013). Moreover, the Nusselt numbers obtained from the

dissipation rates using (2.6)–(2.7) differ from *Nu* computed using (2.5). Therefore, the adequacy of the spatial resolution can also be ensured by comparing the values of *Nu* computed using the aforementioned three methods. In table 1, we list Nu_{ε_u} and Nu_{ε_T} along with *Nu* for all the simulations, and find that they agree reasonably well; the largest difference appears for $Ra = 10^9$, which is due to a limited statistics for this simulation. Furthermore, due to strong variations of the velocity and temperature fields within the BLs, the number of mesh cells should be sufficient in these regions (Shishkina *et al.* 2010). Table 1 shows that the number of grid points within the thermal BL is huge for all the Rayleigh numbers, thus indicating that the thermal BLs are resolved very well in our simulations. In addition, we check the grid-sensitivity by performing simulations for *Ra* equal to 5×10^5, 10^6, 10^7 and 10^9 with different spatial resolutions, and find that the integral quantities, such as the Nusselt and Reynolds numbers, as well as the BL structure, remain nearly the same, which also indicates that our flows are properly resolved.

3. Global transports and flow structure

3.1. *Global quantities*

As we study low-*Pr* convection in a 2-D domain, we first compare the scaling of the global quantities in our simulations with those observed in 3-D RBC for $Pr \approx 0.021$.

The Reynolds number *Re*, which is a measure of the turbulent momentum transport in the flow, is another important global quantity in RBC. We compute *Re* in our flow as

$$Re = \sqrt{Ra/Pr}\, u_{rms}, \tag{3.1}$$

with the rms velocity u_{rms} defined as

$$u_{rms} = \sqrt{\langle u_x^2 + u_z^2 \rangle_{A,t}}. \tag{3.2}$$

Important theoretical models in RBC that yield the scaling relations for global quantities such as *Nu* and *Re* (Shraiman & Siggia 1990; Grossmann & Lohse 2000) assume the existence of a large-scale structure of the order of the size of the cell. For instance, the Shraiman & Siggia (1990) theory provides the scalings of *Nu* and *Re* by considering the properties of (2-D) viscous and thermal BLs generated due to the shear applied by the LSC. Similarly, the Grossmann–Lohse model (Grossmann & Lohse 2000) is based on the existence of an LSC in the convection cell, which is characterized by a single velocity scale. Thus, the above scaling theories are applicable in both 2-D and 3-D RBC (van der Poel *et al.* 2013; Zhu *et al.* 2018). As the LSC also exists in our low-*Pr* 2-D RBC for all the Rayleigh numbers, it is interesting to compare the global quantities in our flow with those observed in 3-D RBC for similar governing parameters, where the LSC structure is also observed.

We compute the Nusselt and Reynolds numbers using (2.5) and (3.1) for all our simulation runs and plot them as a function of *Ra* in figure 1. To compare our *Nu* and *Re* with those obtained in a 3-D RBC, we also show *Nu* and *Re* for $Pr = 0.021$ from Scheel & Schumacher (2017), who investigated low-*Pr* RBC in a cylindrical cell of aspect ratio one from $Ra = 3 \times 10^5$ to $Ra = 4 \times 10^8$. Thus their governing parameters are very similar to the parameters in the present study, and due to the existence of a similar large-scale structure in both these flows, it is interesting to compare the global heat and momentum transports between these flows. Figure 1(*a*) reveals that *Nu* in our 2-D RBC increases as Ra^γ and agrees reasonably well with that of
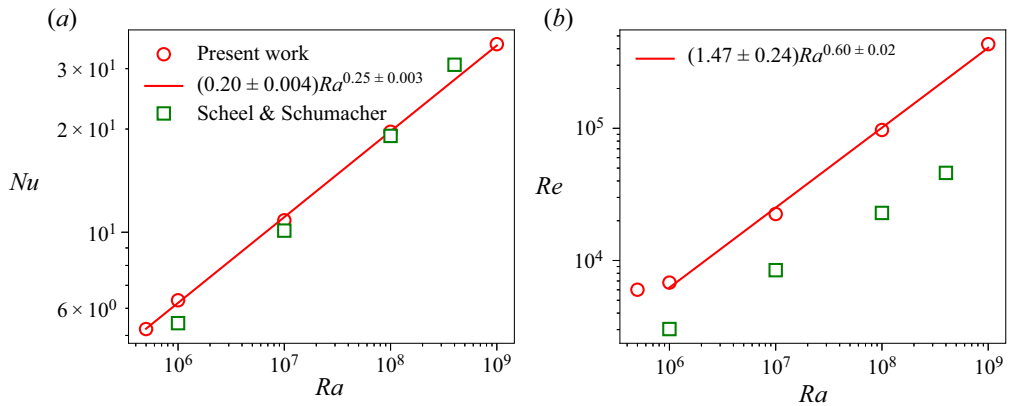
FIGURE 1. The Nusselt and Reynolds numbers as a function of *Ra* in our 2-D RBC (circles) and those obtained by Scheel & Schumacher (2017) for *Pr* = 0.021 in a cylindrical cell of aspect ratio unity (squares). A reasonably good agreement of *Nu* in both 2-D and 3-D RBC for *Pr* = 0.021 is observed.

Scheel & Schumacher (2017). The best fit to our data yields $Nu = (0.20 \pm 0.004)Ra^{0.25 \pm 0.003}$, which is close to $Nu = (0.13 \pm 0.04)Ra^{0.27 \pm 0.01}$ as observed by Scheel & Schumacher (2017) for nearly the same range of *Ra*. The exponent $\gamma = 0.25$ in our flow is smaller than the exponent $\gamma \approx 0.30$ observed for *Pr* = 0.7 and *Pr* = 5.3 in 2-D RBC with a similar flow configuration (Zhang *et al.* 2017b). The lower γ in our low-*Pr* 2-D RBC is similar to that observed in 3-D RBC, where γ also decreases with decreasing *Pr* (Scheel & Schumacher 2017). Note that the Grossmann–Lohse theory (Grossmann & Lohse 2000) also predicts a lower γ for convection in low-*Pr* fluids than for convection in moderate- and high-*Pr* fluids.

We would like to point out that even the magnitudes of *Nu* obtained in our 2-D flows are very similar to those obtained by Scheel & Schumacher (2017). This is remarkable and indicates that, at least in the present range of parameters, the LSC is probably the most dominant mode of heat transport in both the 2-D and the 3-D RBC. Van der Poel *et al.* (2013) also compared *Nu* between 2-D and 3-D RBC with similar flow configurations and noticed that the values of *Nu* at $Ra = 10^8$ are closer in 2-D and 3-D RBC for low Prandtl numbers, whereas a stronger deviation was observed at moderate Prandtl numbers. In an earlier study, however, Schmalzl, Breuer & Hansen (2004) observed that the integral quantities in 2-D and 3-D RBC differ for low Prandtl numbers, whereas they are similar for high Prandtl numbers (van der Poel *et al.* 2013; Pandey *et al.* 2016). However, the sizes of the flow domains in the 2-D and 3-D cases were different, and a smaller $Ra = 10^6$ was used in Schmalzl *et al.* (2004). Interestingly, the scaling $Nu \sim Ra^{0.25}$ in our 2-D RBC agrees well with the existing literature for $Pr \approx 0.021$ in 3-D RBC, as $\gamma \approx 0.25$ has been observed in various earlier investigations (Cioni *et al.* 1997; Glazier *et al.* 1999; Grossmann & Lohse 2000; Pandey & Verma 2016; Zürner *et al.* 2019). Note, however, that the structure and the characteristics of LSC are more complex in 3-D RBC, where it has a quasi-2-D character and exhibits twisting and sloshing modes in addition to azimuthal reorientations in a cylindrical cell (Wagner *et al.* 2012; Schumacher *et al.* 2016; Zwirner *et al.* 2020), which are clearly absent in 2-D RBC. Therefore, the observed similarity between the *Nu–Ra* scaling in our low-*Pr* convection and that in 3-D RBC requires a more detailed investigation, which is beyond the scope of the present work.

Figure 1(*b*) exhibits the Reynolds number in our simulations as a function of *Ra*, along with the *Re* for $Pr = 0.021$ from Scheel & Schumacher (2017). It is clear that the Reynolds numbers in our 2-D RBC are consistently higher than those in the 3-D RBC, for all *Ra*. The best fit in the range of *Ra* from 10^6 to 10^9 yields $Re = (1.47 \pm 0.24)Ra^{0.60 \pm 0.02}$, which is different from the result $Re \sim Ra^{0.45}$ observed in 3-D RBC for $Pr \approx 0.021$ (Pandey & Verma 2016; Scheel & Schumacher 2017). Note that the magnitude of the Reynolds numbers and the exponent in the *Re–Ra* scaling in 2-D RBC have also been observed to be higher than those in 3-D RBC for moderate and high Prandtl numbers (van der Poel *et al.* 2013; Zhang *et al.* 2017*b*). Thus, the exponent in the *Re–Ra* scaling in 2-D RBC appears to remain nearly the same (≈ 0.6) for a wide range of Prandtl numbers (van der Poel *et al.* 2013; Pandey *et al.* 2016; Zhang *et al.* 2017*b*). The larger magnitude of *Re* in our flow is probably due to the more coherent motion of the thermal plumes in 2-D RBC than in 3-D RBC (Zhang *et al.* 2017*a*).

To summarize, the scaling of *Nu* in our 2-D RBC, which is related to the scaling of the mean thermal BL thickness, is very similar to that observed in 3-D RBC for $Pr \approx 0.021$. Therefore, the characteristics of the thermal BL in our 2-D convection may also be similar to those in 3-D RBC for low Prandtl numbers.

3.2. *Flow structure*

The thermal plumes emitted from the top and bottom plates in an RBC cell of aspect ratio around unity move coherently by forming an LSC, which we also detect in our simulations. For all the Rayleigh numbers, we observe that the LSC rotates in a single direction for the entire duration of the simulation and thus does not exhibit any flow reversal (Sugiyama *et al.* 2010; Chandra & Verma 2013; Podvin & Sergent 2015; Pandey *et al.* 2018*b*; Zhang *et al.* 2020). Specifically, in our simulations the LSC rotates in the clockwise direction for $Ra = 10^6$, $Ra = 10^8$ and $Ra = 10^9$, and in the counterclockwise direction for $Ra = 5 \times 10^5$ and $Ra = 10^7$. Therefore, for the consistency of our further analyses and discussions, we transform the horizontal velocity and temperature fields for $Ra = 5 \times 10^5$ and $Ra = 10^7$ by reflecting them about the plane $x = L/2$, which changes the direction of LSC. As a result, the LSC rotates in the clockwise direction in all our simulations.

We exhibit the instantaneous temperature field for $Ra = 10^6$ to $Ra = 10^9$ in figure 2, along with the instantaneous velocity vectors. We observe that because the Kolmogorov and Batchelor length scales decrease with increasing *Re* or *Ra*, the finest thermal structures in the flow, which are coarser for $Ra = 10^6$, become finer with increasing *Ra*. Also, the thickness of the thermal plumes, which are emitted mostly from the bottom left and top right parts of the plates, decreases with increasing *Ra*. This is because the width of the thermal plumes is similar to the thickness of the thermal BLs (Zhou, Sun & Xia 2007; Shishkina & Wagner 2008), which decreases with increasing *Ra*. We also show the time-averaged flow structure for $Ra = 10^6$ to $Ra = 10^9$ in figure 3, which reveals that the mean LSC structure is octagonal (or circular) in our low-*Pr* RBC. The corner flow structures become weaker and the LSC becomes increasingly squarish with increasing *Ra* in our flow. The mean flow structure in our low-*Pr* RBC is different from the mean flow structures in moderate- and high-*Pr* 2-D RBC for similar Rayleigh numbers, where the LSC is usually observed to be aligned along a diagonal of the cell (Sugiyama *et al.* 2010; Zhou *et al.* 2011; Chandra & Verma 2013; Zhang *et al.* 2017*a,b*).

Figure 2 also shows that, in addition to a large-scale structure, smaller structures are also present in the flow. The strengths of the flow structures of various sizes, also known as the flow modes, vary during the evolution of the flow due to the nonlinear interactions
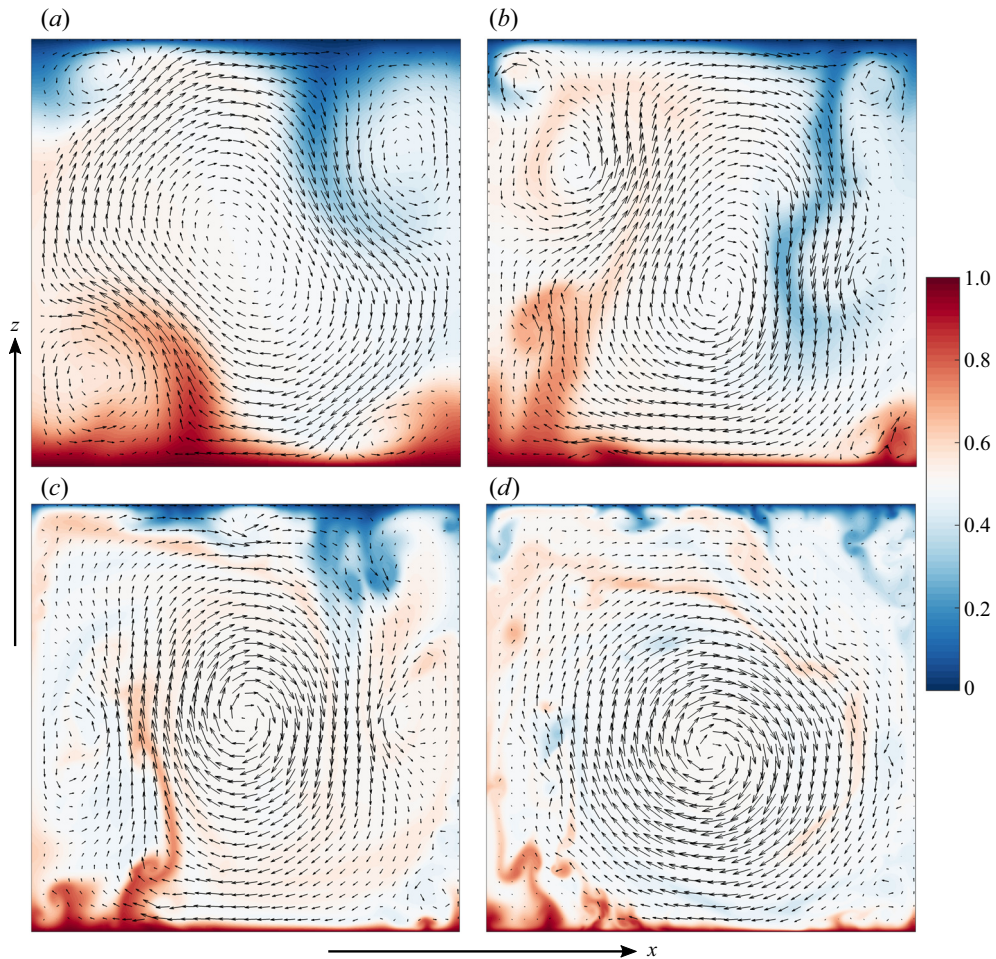
FIGURE 2. Instantaneous temperature (colours) and velocity (vector) fields in the entire simulation domain for (*a*) $Ra = 10^6$, (*b*) $Ra = 10^7$, (*c*) $Ra = 10^8$ and (*d*) $Ra = 10^9$. Increasingly finer thermal structures are observed in the flow with increasing Ra. Also, the primary flow structure, i.e. the LSC, becomes stronger, whereas the secondary structures become weaker with increasing Ra.

(Chandra & Verma 2013). See also the supplementary movies available at https://doi.org/10.1017/jfm.2020.961, which show the temporal evolution of our low-Pr flow for each Ra. We estimate the strengths of various flow modes by computing their kinetic energy content by projecting the velocity field on a sine–cosine basis (Wagner & Shishkina 2013; Chen *et al.* 2019) as follows:

$$u_x(\boldsymbol{x}, t) = \sum_{m,n} \hat{u}_x(m, n, t)[-2\sin(m\pi x)\cos(n\pi z)], \quad (3.3)$$

$$u_z(\boldsymbol{x}, t) = \sum_{m,n} \hat{u}_z(m, n, t)[2\cos(m\pi x)\sin(n\pi z)]. \quad (3.4)$$
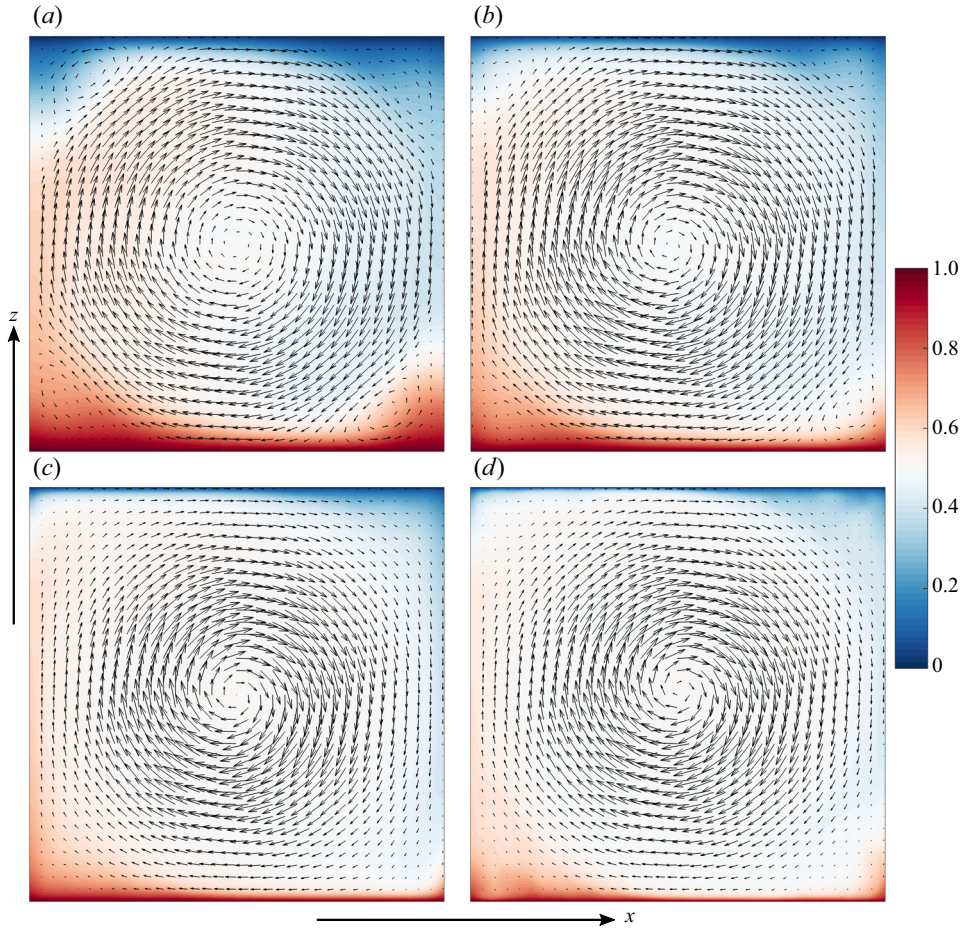
FIGURE 3. Time-averaged flow structure for (*a*) $Ra = 10^6$, (*b*) $Ra = 10^7$, (*c*) $Ra = 10^8$ and (*d*) $Ra = 10^9$. The temperature (colours) and the velocity (vector) fields, averaged for the entire duration of simulations, exhibit that the LSC structure gets increasingly developed, i.e. occupies a larger fraction of the flow domain, with increasing Ra.

Here $m, n \in I$, i.e. they are positive integers. A flow mode with indices (m, n) represents the flow structure with m horizontally-stacked rolls and n vertically-stacked rolls. Thus, the LSC is represented by the $(1, 1)$-mode, and the smaller flow structures, such as the corner rolls, are represented by modes with higher indices (Chandra & Verma 2013; Wagner & Shishkina 2013; Pandey *et al.* 2018*b*; Chen *et al.* 2019). We exhibit the flow structures corresponding to a few dominant modes in our flow in figure 4(*a*–*d*).

The amplitude of the modes is computed as $\hat{u}_x(m, n) = \langle -2u_x(\boldsymbol{x}) \sin(m\pi x) \cos(n\pi z) \rangle_A$ and $\hat{u}_z(m, n) = \langle 2u_z(\boldsymbol{x}) \cos(m\pi x) \sin(n\pi z) \rangle_A$, and the kinetic energy contained in a mode (m, n) is given by

$$E(m, n) = |\hat{u}_x(m, n)|^2 + |\hat{u}_z(m, n)|^2. \tag{3.5}$$

We compute the time-averaged kinetic energy of various flow modes by considering $m, n = 1$–10, and plot the fraction of the total kinetic energy $E = \langle u_x^2 + u_z^2 \rangle_{A,t}$ contained in a few strongest modes in our flow as a function of Ra in figure 4(*e*). Figure 4(*e*) reveals that for $Ra = 5 \times 10^5$, the flow is primarily dominated by one large-scale structure, which
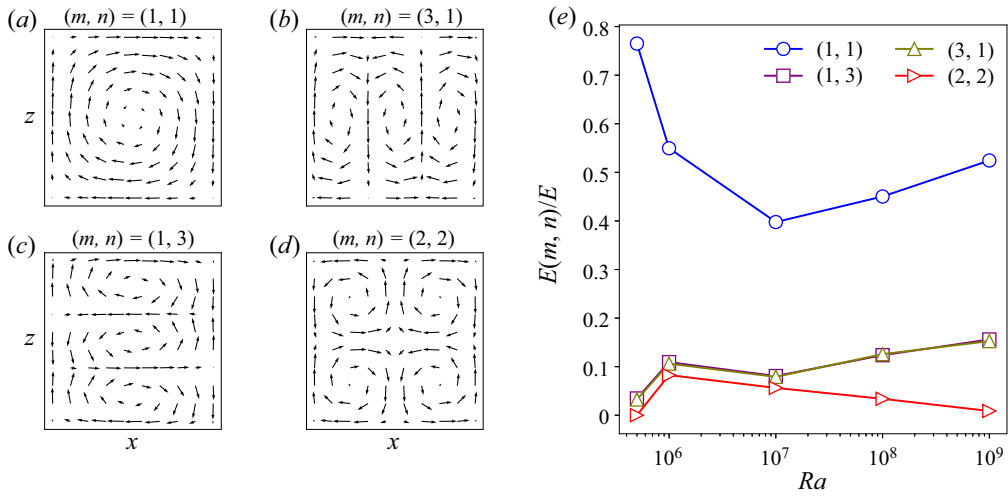
FIGURE 4. Flow structures corresponding to the (*a*) $(1, 1)$-mode, (*b*) $(3, 1)$-mode, (*c*) $(1, 3)$-mode and (*d*) $(2, 2)$-mode. (*e*) Fraction of the total kinetic energy contained in these flow modes as a function of Ra. In the turbulent regime, i.e. for $Ra \geq 10^7$, the strength of the LSC, which is represented by the $(1, 1)$-mode, increases with increasing Ra. Moreover, strong corner flow structures, approximately represented by the $(2,2)$-mode, are present in the flow for $Ra = 10^6$.

becomes weaker for $Ra = 10^6$ due to the growth of the smaller flow structures. This can be confirmed from the supplementary movies and from figure 2(*a*), which show that strong corner flow structures (represented approximately by the $(2,2)$-mode) are present in the flow at $Ra = 10^6$. The strength of the LSC further decreases for $Ra = 10^7$ as even smaller structures are generated due to the increased Reynolds number of the flow. However, for $Ra \geq 10^7$, the strength of the LSC (i.e. of the $(1,1)$-mode) grows and the total strength of the small-scale structures decays with increasing Ra (Sugiyama *et al.* 2010; Chandra & Verma 2013). This indicates that with increasing Ra the LSC structure gets more and more squarish and increasingly fills the entire domain in our low-Pr RBC (Lui & Xia 1998; Niemela & Sreenivasan 2003).

Furthermore, we observe that the evolution of the flow for $Ra = 5 \times 10^5$ is unsteady and periodic time-dependent, while for $Ra = 10^6$ it is nearly periodic, i.e. some non-periodicity sets in the flow. To depict this, we look at the time trace of the temperature field at a fixed probe in the flow. Figure 5 shows a segment of the temperature trace at a probe located at the centre of the bottom plate near the thermal BL height, i.e. at $x_0 = L/2$, $z_0 \approx \delta_{\langle T \rangle}$. Figure 5(*a*) reveals that the temperature signal is periodic for $Ra = 5 \times 10^5$, whereas figure 5(*b*) shows that some non-periodicity appears in the signal for $Ra = 10^6$. The temperature field at the probe for $Ra \geq 10^7$ varies chaotically, indicating that the flow for $Ra \geq 10^7$ is turbulent (see also supplementary movies).

Unlike the flow in a pipe or channel, the RBC flow in a confined domain is not homogeneous in the horizontal directions. Instead, the horizontal plates can be divided into three distinct flow regions. For RBC in a domain of aspect ratio around unity, the hot plumes are generated primarily near one of the sidewalls and ascend towards the cold plate along that sidewall. Similarly, the cold plumes detaching from the top plate descend towards the hot plate along the opposite sidewall. These two regions are called respectively
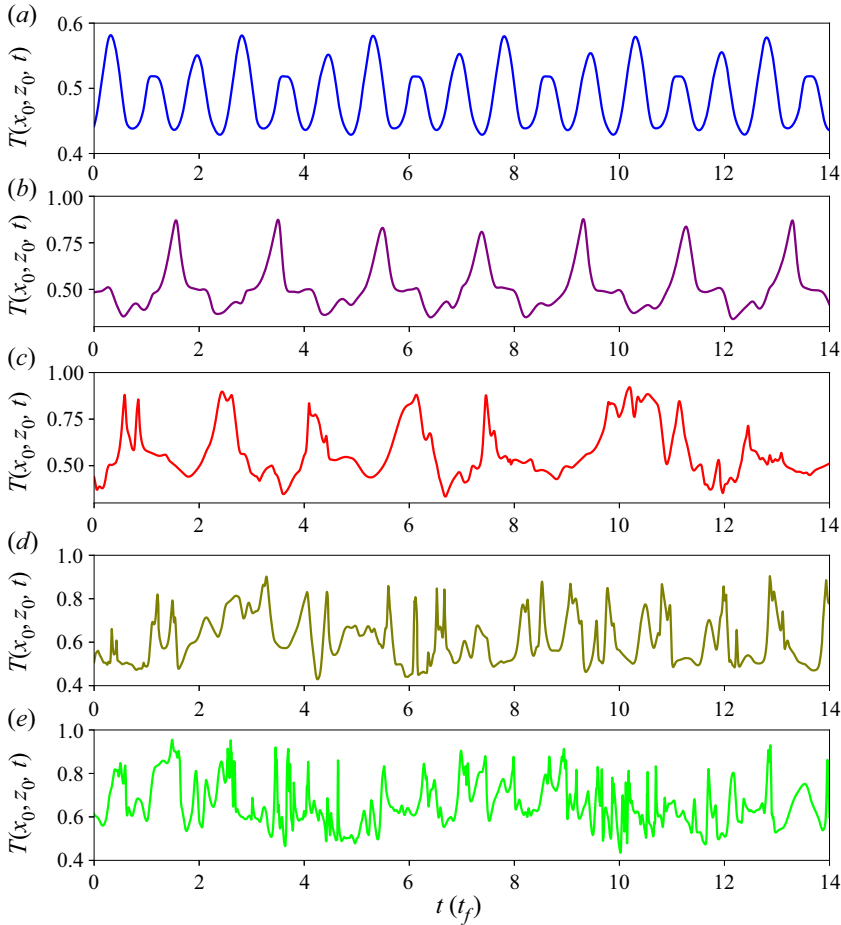
FIGURE 5. A segment of the time traces of the temperature field at a fixed probe near the centre of the bottom plate at the thermal BL height, i.e. at $x_0 = L/2$, $z_0 \approx \delta_{\langle T \rangle}$, for (a) $Ra = 5 \times 10^5$, (b) $Ra = 10^6$, (c) $Ra = 10^7$, (d) $Ra = 10^8$ and (e) $Ra = 10^9$ (taken from run 5a). Panel (a) shows that the flow is periodic for $Ra = 5 \times 10^5$, whereas the flow is nearly periodic for $Ra = 10^6$, as indicated by the signal in panel (b). The temperature at the probe varies chaotically in (c–e), indicating that the flow is turbulent for $Ra \geq 10^7$.

the plume-ejection and plume-impact regions (van der Poel *et al.* 2015; Schumacher *et al.* 2016; Zhu *et al.* 2018). In between these two regions, there exists a shear-dominated region, where the LSC is nearly parallel to the horizontal plates. We also depict these regions in our flow in a caricature in figure 6. Due to this specific flow morphology of RBC in a confined domain, the thermal and viscous BL profiles have often been studied in the shear-dominated central region (Zhou *et al.* 2010; van der Poel *et al.* 2013; Schumacher *et al.* 2016; Wang *et al.* 2018). In this study, however, we compute the local temperature profiles in the aforementioned three regions and find that the BL profiles in the shear and impact regions are similar, and differ from the profiles in the ejection region.
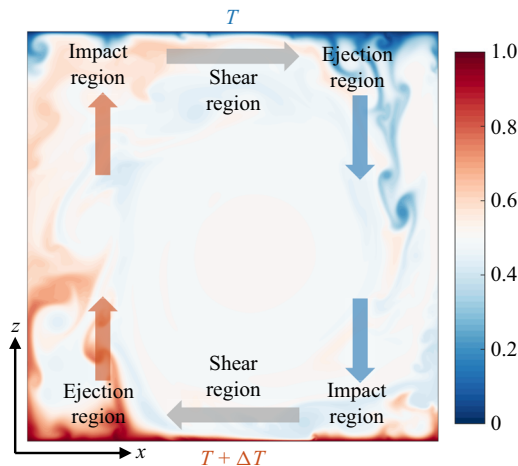
FIGURE 6. A caricature exhibiting the plume-ejection, shear-dominated and plume-impact regions at the top and bottom plates in our low-Pr 2-D RBC. An instantaneous snapshot of the temperature field for $Ra = 10^9$ is used to depict these regions.

4. Thermal boundary layer thicknesses

In this section, we discuss the scaling of the thermal BL width computed using the local as well as the horizontally-averaged temperature profiles.

4.1. *Local boundary layer thicknesses*

We observe for all Ra that the central region near the plates is dominated by shear generated due to LSC, and therefore, the flow properties at $x \approx L/2$ are similar to those in a shear flow. The locations $x = L/4$ and $x = 3L/4$ at the bottom plate in our flow approximately correspond to the plume-ejection and plume-impact regions; i.e. the hot plumes are ejected from the bottom plate mostly at $x \approx L/4$ and the cold plumes impact at the bottom plate mostly at $x \approx 3L/4$ (see figure 2). The situation is reversed at the top plate; i.e. the physical location of the ejection region at the bottom corresponds to the impact region at the top, and vice versa. (See also figure 6, where we have summarized these flow regions at the plates in a caricature.) We have analysed the properties of the temperature profiles measured at several locations in the flow. However, for clarity, we will mainly discuss the profiles measured at $x = L/4$, $x = L/2$ and $x = 3L/4$, as these positions at the bottom plate typically correspond to the ejection, shear and impact regions, respectively. We would like to point out that the large-scale structures in our flow fluctuate strongly in time (see supplementary movies), which causes the flow properties at the aforementioned locations to be occasionally influenced by the properties from the other regions. Therefore, we inevitably sample a mixed statistics due to the use of an immovable observational window in the flow.

We show the time-averaged temperature profiles at $x = L/4$, $x = L/2$ and $x = 3L/4$ for $Ra = 10^6$ to $Ra = 10^9$ in figure 7. To reduce the scatter, we average the profiles in a tiny neighbourhood around the aforementioned locations. Specifically, the profile at x_0 is averaged in the region corresponding to $x_0 - 0.02L \leq x \leq x_0 + 0.02L$, where $x_0 = L/4, L/2, 3L/4$. Figure 7 shows that the profiles at $x = L/2$ are nearly symmetric about the midplane, as $x \approx L/2$ corresponds to the shear-dominated region at both the
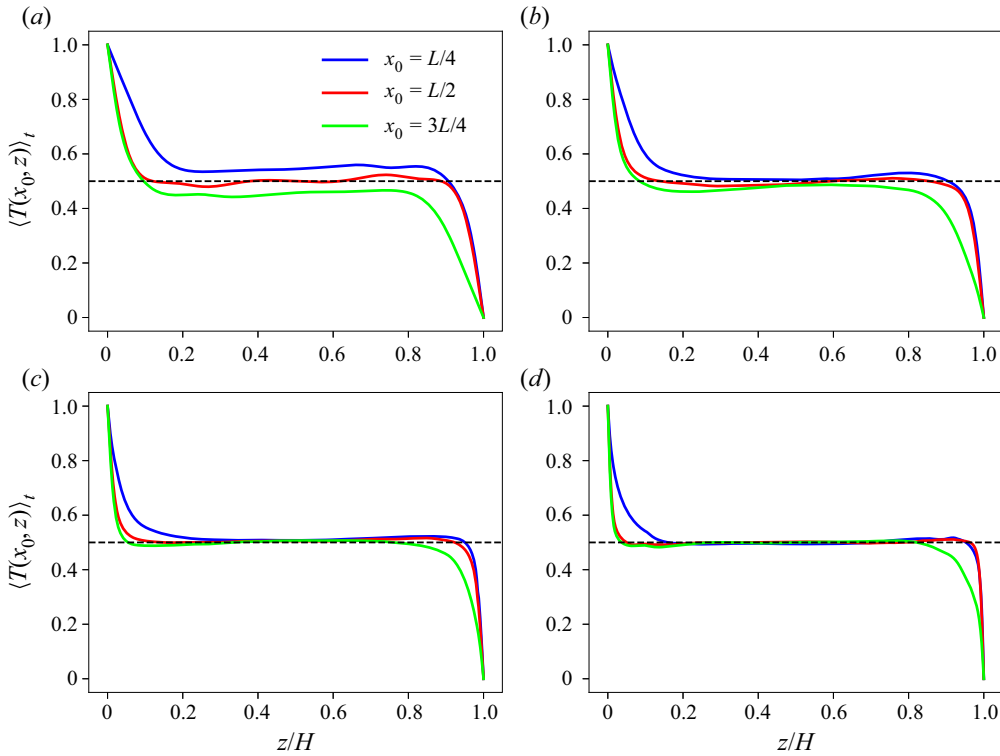
FIGURE 7. Time-averaged temperature profiles measured at different horizontal positions for (a) $Ra = 10^6$, (b) $Ra = 10^7$, (c) $Ra = 10^8$ and (d) $Ra = 10^9$. For all Ra, profiles at $x = L/2$ are symmetric about the midplane, whereas those at $x \neq L/2$ do not exhibit symmetry, because of the differing flow properties at the opposite plates at the particular physical location. In all the panels, blue curves near the bottom plate are similar to green curves near the top plate, and vice versa.

top and bottom plates. The profiles at $x \neq L/2$, however, are not symmetric about the midplane. For instance, we can see in figure 7(d) for $Ra = 10^9$ that the profile near the bottom (top) plate at $x = L/4$ ($x = 3L/4$), which corresponds to the ejection region, approaches the bulk temperature slowly compared to the profiles in the other two regions. This is because the hot (cold) plumes that are ejected from the bottom (top) plate in the ejection region carry their thermal energy for a longer time and travel farther in the bulk region before losing their heat due to thermal diffusion. Moreover, the profile near the bottom (top) plate at $x = 3L/4$ ($x = L/4$), which corresponds to the impact region, looks similar to that at $x = L/2$ in the shear region. Figure 7 shows that the local profiles for all the Rayleigh numbers exhibit similar behaviour. Thus, to conclude, the temperature profiles in the impact and shear regions are similar, whereas the temperature profile in the ejection region differs from them. Therefore, from now on, we will discuss the properties of the temperature profiles based on whether they belong to the impact, ejection or shear region, and not based on their physical location in the flow domain.

We compute the local thermal BL width $\delta_T(x)$ using the slope method (Zhou *et al.* 2011; Scheel *et al.* 2012; Wagner *et al.* 2012), where $\delta_T(x)$ is estimated as the distance from the plate where the slope of the temperature profile drawn at the plate meets the horizontal line passing through the first minimum of the profile. In figure 8, we demonstrate this
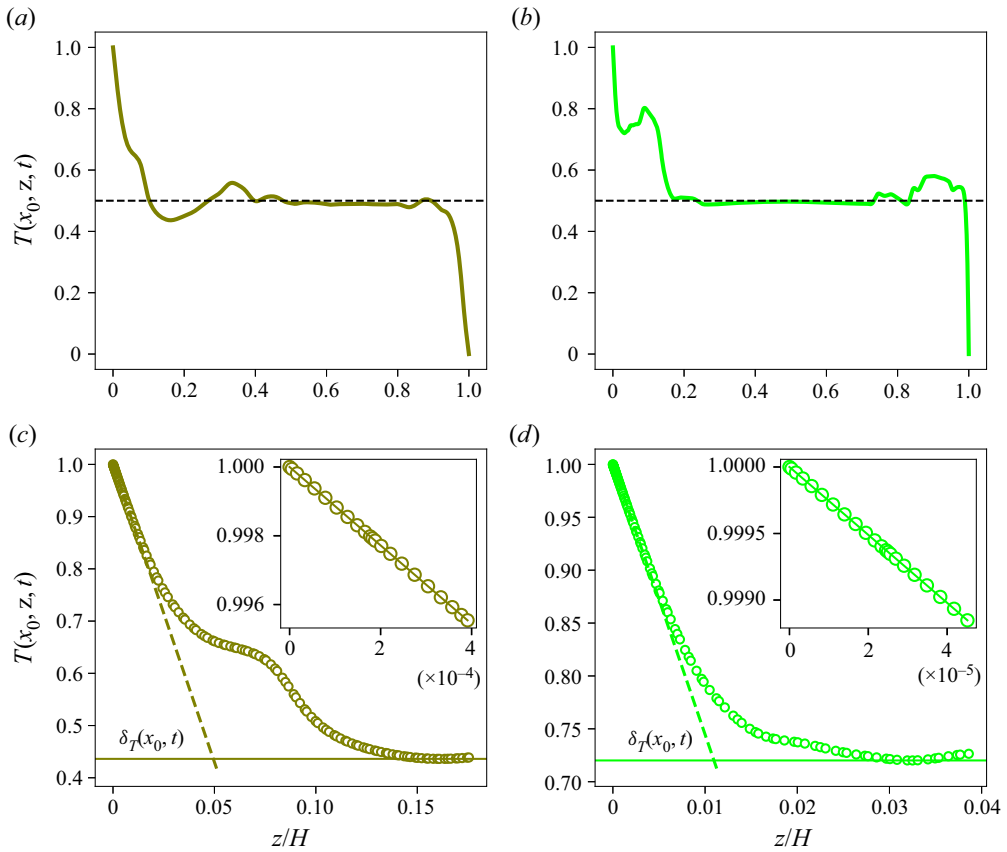
FIGURE 8. Instantaneous local temperature profiles (*a,b*) and their magnifications near the bottom plate (*c,d*) to demonstrate the determination of the instantaneous local thermal BL thickness using the slope method. Panels (*a*) and (*c*) show a profile measured in the shear-dominated region at $x_0 = L/2$ for $Ra = 10^8$; panels (*b*) and (*d*) show a profile measured in the plume-ejection region at $x_0 = L/4$ for $Ra = 10^9$. Position of the intersection of the horizontal line drawn at the first minimum with the slope at the plate yields $\delta_T(x_0, t)$. Panels (*a*) and (*b*) show that the temperature at the first minimum may differ from $T_{bulk} = \Delta T/2$. Inset in (*c,d*) indicates the linear variation of temperature in the vicinity of the bottom plate.

method of determining the BL thickness from the instantaneous temperature profiles measured at two different positions at the plate. Figure 8 shows that the profiles do not always approach the bulk temperature monotonically, and the first minimum may differ from the bulk temperature. We also compute the instantaneous BL thicknesses using the local vertical temperature gradient at the plate as $\delta_T(x) = 0.5/|\partial T(x)/\partial z|_{z=0}$, which is equivalent to computing the BL thickness using the slope method with the horizontal line drawn at the mean temperature $\Delta T/2$. We find that the mean (and most of the time instantaneous) BL thicknesses determined using this method are nearly the same as those obtained using the first minimum method. However, we prefer the first minimum method to include the instantaneous variation of the profiles, as the temperature in the bulk region may instantaneously differ from $\Delta T/2$.

To explore the structure of the thermal BL, we compute the local BL thicknesses $\delta_{\langle T \rangle}(x)$ at both the plates using the time-averaged temperature profiles. Figure 9 shows the local
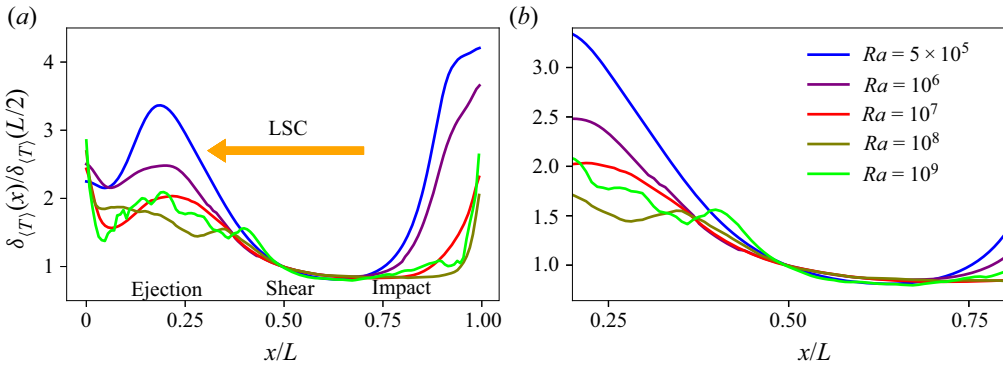
FIGURE 9. (*a*) Variation of the normalized local BL thicknesses along the horizontal plate computed using the time-averaged profiles. Except very close to the sidewalls, the local thicknesses $\delta_{\langle T \rangle}(x)$ are larger in the ejection region and decrease as the impact region is approached; i.e. the thickness grows in the direction of LSC. (*b*) Magnification of (*a*) exhibiting the BL structure in the central region away from the sidewalls, which shows that the BL structure is nearly independent of *Ra* in the impact and shear regions.

BL width averaged over the top and bottom plates and normalized with the BL width at $x = L/2$. Note that due to the interchange of the ejection and impact regions, local BL thickness at a position x in figure 9 is the average of $\delta_{\langle T \rangle}(x)$ at the bottom and $\delta_{\langle T \rangle}(L - x)$ at the top plate. Figure 9 reveals that the BL structure is similar for all the explored *Ra* in our low-*Pr* RBC. We observe that $\delta_{\langle T \rangle}(x)$ is the largest near the sidewalls and decreases as one moves towards the central region. Moreover, the local thicknesses are larger in the ejection region than in the other two regions, as indicated in figure 9(*a*). We also find that the values of $\delta_{\langle T \rangle}(x)$ in the impact region are a bit smaller than those in the shear region. To show the BL structure away from the sidewalls, we plot $\delta_{\langle T \rangle}(x)$ for $0.2L \leq x \leq 0.8L$ in figure 9(*b*), which reveals that the BL structure is nearly independent of *Ra* in the impact and shear regions. In the ejection region, however, the variation of the normalized BL thickness depends on *Ra*. We quantify the relative variation of the BL thicknesses exhibited in figure 9(*b*) as

$$\mathcal{R} = \frac{[\delta_{\langle T \rangle}(x)]_{max} - [\delta_{\langle T \rangle}(x)]_{min}}{[\delta_{\langle T \rangle}(x)]_{min}}, \tag{4.1}$$

where $[\delta_{\langle T \rangle}(x)]_{max}$ and $[\delta_{\langle T \rangle}(x)]_{min}$ are respectively the maximum and minimum BL thicknesses over the central region, i.e. in the region $0.2L \leq x \leq 0.8L$ at the plate. We find $\mathcal{R} = 3.1, 1.9, 1.5, 1.0, 1.6$ respectively for $Ra = 5 \times 10^5, 10^6, 10^7, 10^8, 10^9$, which indicates that $\mathcal{R}$ generally decreases with increasing *Ra* in our flow. Our data at $Ra = 10^9$ do not follow the decreasing trend very well, which might be due to a limited statistics available for this *Ra*. A few more simulations at intermediate Rayleigh numbers would probably yield a better picture of the BL structure in the ejection region in our low-*Pr* flow.

According to the Prandtl–Blasius BL theory, the BL thickness grows as $\sqrt{x}$ in the downstream direction for a laminar BL, whereas it grows linearly with x for a turbulent BL (Schlichting & Gersten 2004). In our 2-D RBC, the hotter or colder fluid impinges on the plate in the impact region and then moves along the plate towards the ejection region. We thus also observe a growth of the BL thickness in the downstream direction, i.e. in the direction of the LSC on the plate. However, $\delta_{\langle T \rangle}(x)$ in our low-*Pr* RBC does not
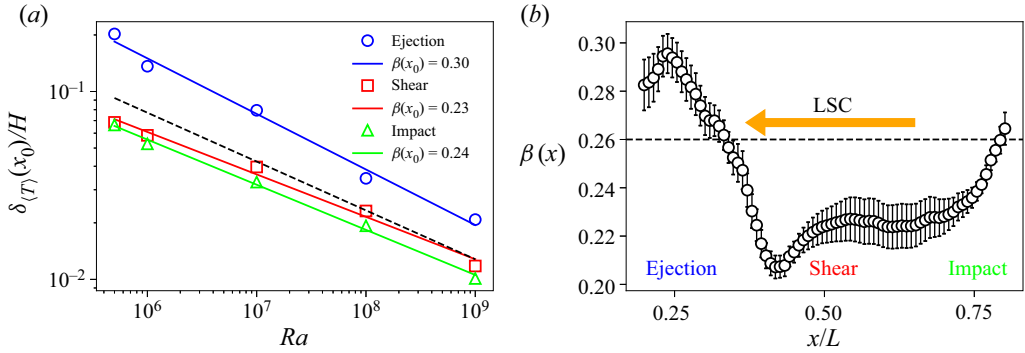
FIGURE 10. (*a*) Local thermal BL thicknesses averaged over both the plates vary as $Ra^{-\beta(x)}$ in the ejection, shear and impact regions, with $\beta(x_0)$ being larger in the ejection region. The black dashed line indicates the scaling of the BL thickness $\delta_{\langle T \rangle}$ computed using the horizontally- and temporally-averaged profiles (shown in figure 12*b*). If these scalings hold for the larger Rayleigh numbers, the blue line will intersect the red or green line at $Ra^* \approx 8 \times 10^{12}$, beyond which the thermal BL might become uniform at the plate. (*b*) Variation of the local scaling exponent $\beta(x)$ along the plate obtained from the BL thicknesses averaged over the top and bottom plates. The dashed horizontal line indicates the scaling exponent of the mean BL thickness. The direction of LSC and the ejection, shear and impact regions are also indicated.

follow either of the aforementioned scalings. Possible reasons for a different BL structure in our flow might be the assumptions in the Prandtl–Blasius BL theory, which are not totally satisfied in our 2-D convection flow. For example, the BLs in our flow are not entirely laminar and the turbulent fluctuations within the BL region become stronger with increasing Ra (see figure 16*b*). We moreover observe that the BL structure is not symmetric about the centre of the plate, which is qualitatively similar to observations made for high-Pr 2-D RBC (Werne 1993; Zhou *et al.* 2011). Our observations of the BL structure in our low-Pr convection are also qualitatively similar to those of Wagner *et al.* (2012) in a cylindrical cell of aspect ratio one, where the BL width increases in the direction of LSC, as well as to the observations of Scheel & Schumacher (2014) that the local BL widths are larger in the plume-ejection region. Wagner *et al.* (2012), however, observed a nearly linear growth of the BL thickness along the direction of LSC. Our results are also different from those of Lui & Xia (1998), who studied the thermal BL structure in a cylindrical cell of aspect ratio one filled with water and observed that, in the plane of LSC, the BL width is minimum at the centre of the plate and increases symmetrically towards the sidewalls. The aforementioned differences between the BL structure in our 2-D RBC and those observed in 3-D RBC, therefore, indicate that the quasi-2-D nature and other characteristics of LSC in 3-D RBC also affect the BL structure.

We compute the local thermal BL thicknesses $\delta_{\langle T \rangle}(x_0)$ at $x_0 = L/4$, $x_0 = L/2$ and $x_0 = 3L/4$ using the time-averaged profiles exhibited in figure 7 and find that $\delta_{\langle T \rangle}(x_0)$ decreases with increasing Ra as $Ra^{-\beta(x_0)}$, with the exponent $\beta(x_0)$ depending on the position at the plate. In figure 10(*a*), we plot $\delta_{\langle T \rangle}(x_0)$ averaged over the corresponding regions at the top and bottom plates as a function of Ra, which reveals that the BL thicknesses in the impact and shear regions are similar for all Ra. This is consistent with the fact that the profiles in the shear and impact regions exhibited in figure 7 are also similar. The best fit yields that $\delta_{\langle T \rangle}(x_0)/H$ varies as $(1.4 \pm 0.2)Ra^{-0.23 \pm 0.01}$ in the shear region and as $(1.5 \pm 0.1)Ra^{-0.24 \pm 0.01}$ in the impact region. The local BL thicknesses in
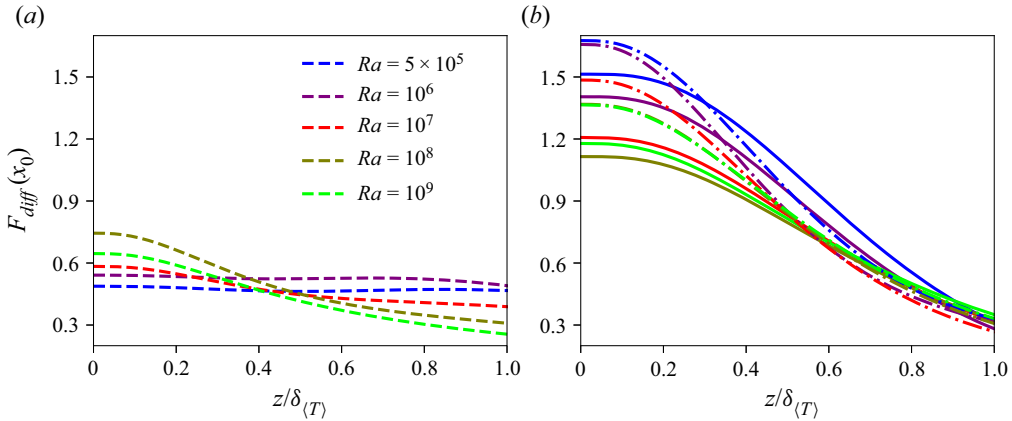
FIGURE 11. Vertical profiles of the fraction $F_{diff}(x_0)$ of the total heat flux carried by the thermal diffusion in (*a*) the ejection region and (*b*) the shear region (solid curves) and impact region (dash-dot curves) within the BL. The values of $F_{diff}(x_0)$ at the plate are smaller in the ejection region than in the shear and impact regions, and with increasing Ra, $F_{diff}(x_0)$ is generally increasing in the ejection region and decreasing in the other two regions.

the ejection region, however, are larger than those in the other two regions for all Ra, and scale as $(8.9 \pm 1.1)Ra^{-0.30 \pm 0.02}$.

We further explore the variation of the local exponent $\beta(x)$ at the plate by computing it from the local BL thicknesses. Figure 10(*b*) exhibits the local exponents $\beta(x)$ computed from the averaged BL thicknesses at both the plates in the central region far from the sidewalls. We observe that the $\beta(x)$ values are larger in the ejection region than in the shear and impact regions, where they are nearly the same. Note that the thermal BL thickness is related to the diffusive heat flux at the plate. To understand the position-dependent variation of the properties of the thermal BL, we compute the diffusive fraction of the total heat flux as $F_{diff}(x_0) = (H\partial\langle T\rangle_t(x_0)/\partial z)/(Nu\Delta T)$ in the ejection, shear and impact regions. Figure 11(*a*) shows $F_{diff}(x_0)$ as a function of $z/\delta_{\langle T\rangle}$ in the ejection region, while figure 11(*b*) shows $F_{diff}(x_0)$ in the shear region (solid curves) and the impact region (dash-dot curves). We observe for all Ra that the values of $F_{diff}(x_0)$ at the plate and in its vicinity in the ejection region are smaller than those in the shear region, which in turn, are a bit smaller than those in the impact region. This is because of a larger temperature gradient in the impact region due to impinging cold (hot) plumes at the bottom (top) plate. As the BL width is inversely proportional to the vertical temperature gradient (or the diffusive flux) at the plate, this implies that the local BL thickness in the ejection region is larger than the thicknesses in the shear and impact regions, which is consistent with the BL structure from figure 9.

Furthermore, we observe that $F_{diff}(x_0)$ in the vicinity of the plate is generally increasing in the ejection region, but decreasing in the shear and impact regions, with increasing Ra. This means that with increasing Ra, the BL width in the ejection region decreases faster, whereas the BL widths in the other two regions decrease slower, compared to the mean BL thickness, which agrees with the observations of figure 10. Therefore, for moderately large Rayleigh numbers in our low-Pr flow, the difference between the diffusive contributions from various regions is decreasing, or, in other words, the variation of the diffusive heat flux over the plate becomes weaker with increasing Ra. The reason for this weaker

variation is the increasing strength of LSC with increasing *Ra* in our flow (Lui & Xia 1998), as we have observed that the (1,1)-mode representing the LSC structure becomes stronger as *Ra* increases (see figure 4*e*). A stronger LSC causes the cold (hot) plumes impinging on the bottom (top) plate in the impact region to move a larger distance along the plate before their heat is lost due to thermal diffusion. This causes an increasingly uniform temperature gradient along the plate with increasing *Ra*. If the observed trend in our flow continues to hold for larger *Ra*, the local heat flux in the ejection region might take over those in the other two regions for large enough *Ra*. This picture would be consistent with the findings of Zhu *et al.* (2018) in 2-D RBC for $Pr = 1$, $Ra > 10^{11}$, that the local heat flux at the plate is larger in the ejection region. Figure 11 additionally shows that the variation of $F_{diff}(x_0)$ for $z \geq 0.4\delta_{\langle T \rangle}$ becomes nearly independent of *Ra* in the shear and impact regions, whereas $F_{diff}(x_0)$ generally decreases with increasing *Ra* in the ejection region. This, in turn, suggests that away from the plate but within the BL region, the turbulent fraction of the heat flux in the ejection region increases with increasing *Ra*. Combining the above scenarios, our results suggest that in the whole BL the local heat flux in the ejection region becomes stronger with increasing *Ra* in our low-*Pr* convection.

Thus, the difference between the local thicknesses in the ejection region and the other two regions decreases with increasing *Ra*, and, if the present trends hold also for the larger Rayleigh numbers, the local thicknesses for sufficiently large *Ra* might become independent of the horizontal position. We can estimate this asymptotic *Ra* by finding the intersection point of the blue line with either the red or the green line in figure 10. We find that these lines will intersect at $Ra^* \approx 8 \times 10^{12}$, and therefore, the thermal BL structure in our low-*Pr* convection might become uniform for $Ra \geq Ra^*$. If we take the error bars into account, Ra^* may vary between 5×10^9 and 2×10^{19}, and thus the predicted range of Ra^* is very wide. Note that the estimated Ra^* is very large and would probably correspond to the *ultimate regime of convection* for this Prandtl number (Scheel & Schumacher 2017). Scheel & Schumacher (2017) used various methods to predict the onset of the ultimate regime in a cylindrical cell of aspect ratio one and found interestingly that the onset for $Pr = 0.021$ may occur between $Ra = 5 \times 10^9$ and $Ra = 10^{18}$. Lui & Xia (1998) and Wang & Xia (2003) studied the thermal BL structure in water for high Rayleigh numbers and also observed that in the direction of LSC the variation of the local BL thickness with the horizontal position becomes weaker with increasing *Ra*.

In the next section, we discuss the scaling of the mean BL thickness at the plates.

4.2. *Mean boundary layer thickness*

In RBC, the horizontally-averaged temperature varies primarily in the thin thermal BLs and remains almost constant in the bulk region. We compute the horizontally- and temporally-averaged temperature $\langle T \rangle_{x,t}$ for all *Ra* and plot them in figure 12(*a*), which shows that the mean temperature in the bulk is indeed approximately a constant. Figure 12(*a*) shows the profiles averaged over the bottom and top halves of the domain, as they are symmetric about the midplane ($z = 0.5H$) due to the Oberbeck–Boussinesq convection in the present case. We observe that the profiles approach the bulk temperature increasingly faster as *Ra* increases, thus indicating that the diffusive region, where the vertical temperature gradient is significant, shrinks with increasing *Ra*.

We compute the mean thermal BL width $\delta_{\langle T \rangle}$ from $\langle T \rangle_{x,t}$ using the slope method, and we plot the average thickness of the top and bottom BLs as a function of *Ra* in figure 12(*b*), which shows that the average thickness decreases with increasing *Ra* as $\delta_{\langle T \rangle}/H = (2.8 \pm 0.1)Ra^{-0.26 \pm 0.004}$. As previously mentioned, the mean thermal BL thickness is related to *Nu* by $\delta_{\langle T \rangle}/H = 0.5/Nu$. This is because the diffusive contribution to
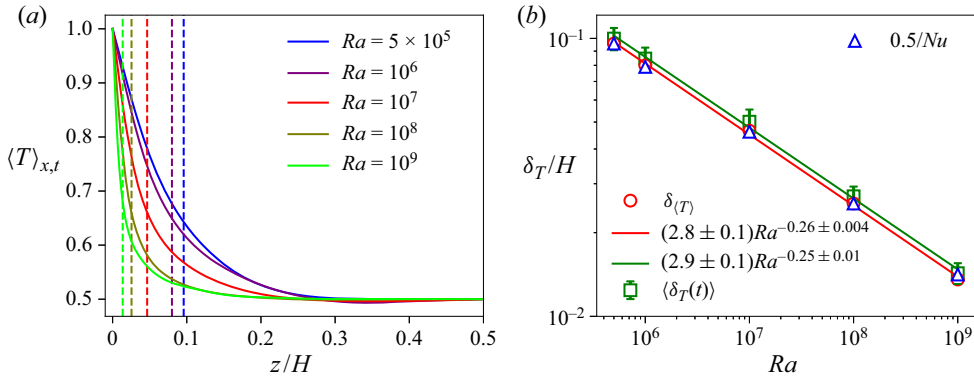
FIGURE 12. (*a*) Horizontally- and temporally-averaged temperature profiles for all the Rayleigh numbers exhibit that the bulk fluid is mixed well and $T_{bulk} \approx \Delta T/2 = 0.5$. (*b*) Mean thickness of the top and bottom thermal BLs decreases as $Ra^{-0.26}$. We show the thickness $\delta_{\langle T \rangle}$ computed from the time-averaged profiles as well as the time-averaged thickness $\langle \delta_T(t) \rangle$ computed from the instantaneous profiles, with the error bars in $\langle \delta_T(t) \rangle$ indicating the standard deviation of $\delta_T(t)$. Mean thermal BL thicknesses computed from the relation $\delta_{\langle T \rangle} = 0.5H/Nu$ are also indicated as blue triangles. Dashed vertical lines in (*a*) indicate $\delta_{\langle T \rangle}$ for all Ra with the corresponding colours.

the total heat transport decreases with increasing Nu, and thus, the region where diffusive processes are dominant shrinks as Nu increases. Therefore, we also show the BL thickness computed as $0.5/Nu$ in figure 12(*b*), and observe excellent agreement with the thickness computed using the slope method. We also compute the thermal BL widths $\delta_T(t)$ from the instantaneous horizontally-averaged temperature profiles and average them to obtain the mean width $\langle \delta_T(t) \rangle$, which is also plotted in figure 12(*b*). We observe that $\langle \delta_T(t) \rangle$ is slightly larger than $\delta_{\langle T \rangle}$ for all Ra, but its variation with Ra is nearly the same. The best fit yields $\langle \delta_T(t) \rangle / H = (2.9 \pm 0.1)Ra^{-0.25 \pm 0.01}$, which agrees very well with $\delta_{\langle T \rangle}$ as computed from the time-averaged profiles.

The BLs in our low-*Pr* RBC are not completely laminar and exhibit fluctuations for all the Rayleigh numbers. Therefore, we compute the rms temperature fluctuations from the mean temperature profile $\langle T \rangle_{x,t}$ as

$$\sigma_T(z) = \sqrt{\langle (T - \langle T \rangle_{x,t})^2 \rangle_{x,t}} \qquad (4.2)$$

and plot $\sigma_T(z)$ averaged over the top and bottom halves of the domain in figure 13(*a*). We observe that the rms fluctuations increase with increasing distance from the plate and attain their maximum value near the edge of the thermal BL (Deardorff & Willis 1967; Wang & Xia 2003; Zhou & Xia 2013). This is due to the generation and perpetual emission of thermal plumes inside the thermal BL. Note that the thickness of the plumes is similar to the thickness of the thermal BL, and their temperature is higher than that of the ambient fluid within the bottom thermal BL (Zhou *et al.* 2007; Shishkina & Wagner 2008). Therefore, the decrease of the horizontally-averaged temperature with increasing distance from the bottom plate is primarily due to the decreasing temperature of the ambient fluid, as the plumes almost entirely retain their heat or temperature within the BL region. Thus, the disparity between the temperatures of the ambient fluid and the plumes increases with increasing distance from the bottom plate, which causes the increase of $\sigma_T(z)$ within the thermal BL. A similar difference between the temperatures of the cold plumes and the ambient fluid in the top thermal BL causes the increase of $\sigma_T(z)$ near the top plate.
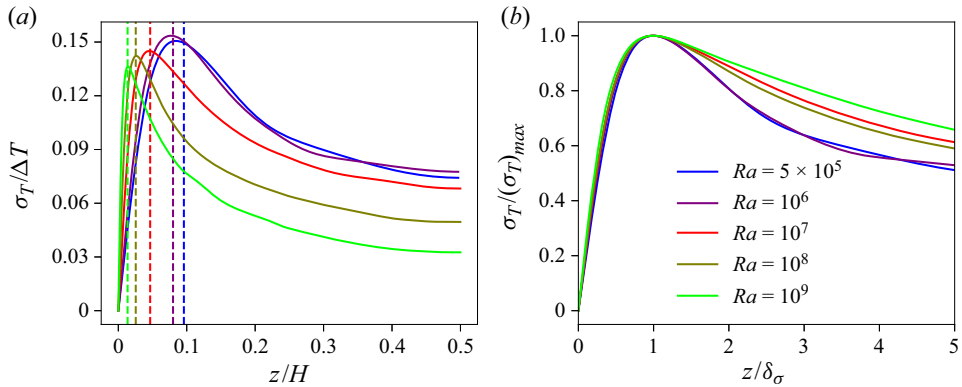
FIGURE 13. (*a*) Vertical profiles of the rms temperature fluctuations averaged over the top and bottom halves of the domain for all *Ra* attain their maximum value near the edge of the thermal BL and then decay monotonically in the bulk region towards the centre. Dashed vertical lines with the corresponding colours indicate the mean BL thicknesses $\delta_{\langle T \rangle}$. (*b*) Profiles normalized with their maximum value as a function of the normalized vertical distance collapse reasonably well within the thermal BL region.
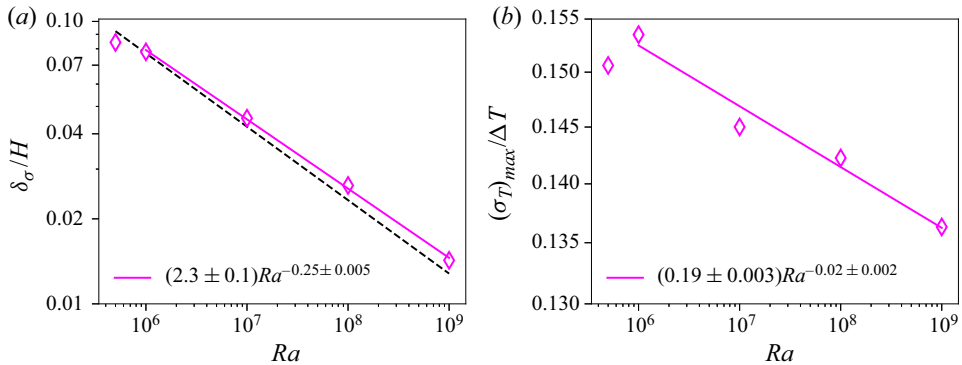

FIGURE 14. (*a*) Thermal BL thickness extracted from the temperature variance profiles scales with *Ra* similarly to the scaling of $\delta_{\langle T \rangle}(Ra)$, which is indicated by a black dashed line. (*b*) The maximum amplitude of the rms temperature fluctuations for $Ra \geq 10^6$ decreases very weakly with increasing *Ra*.

After attaining the maximum, the rms fluctuations decline monotonically as the central region of the flow is approached. This is because the plumes are not able to retain their temperature due to increased turbulent mixing outside the BL region.

Therefore, it is clear from figure 13(*a*) that the position of the maximum of σ_T also yields a measure of the BL thickness (Wang & Xia 2003; Zhou & Xia 2013). We observe that both δ_σ (the position corresponding to the maximum of σ_T) and the maximum amplitude of the fluctuations decrease with increasing *Ra*. We therefore show the normalized temperature variance profiles $\sigma_T/(\sigma_T)_{max}$ as a function of the normalized distance z/δ_σ in figure 13(*b*), and find that the normalized profiles collapse reasonably well within the BL region, i.e. up to $z \approx \delta_\sigma$ (Zhou & Xia 2013). However, the profiles do not seem to collapse outside the BL region. This indicates that δ_σ is indeed a characteristic length scale within the thermal BL region. We plot δ_σ as a function of *Ra* in figure 14(*a*) and observe that δ_σ
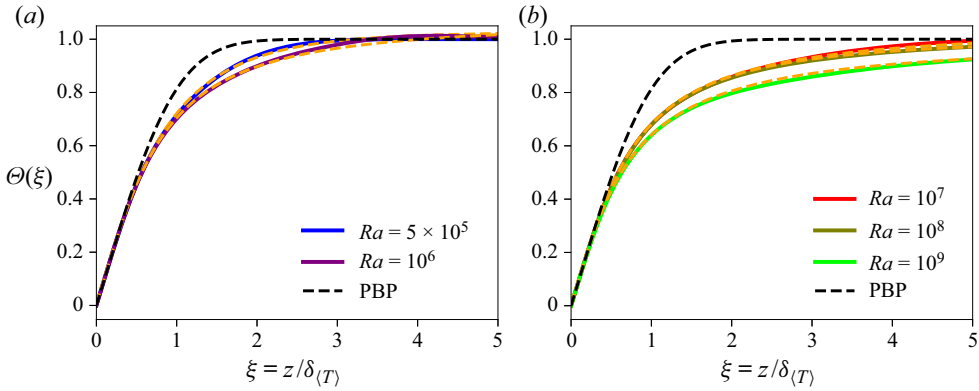
FIGURE 15. BL profiles of the horizontally- and temporally-averaged temperature Θ deviate from the PBP profile (black dashed curve in both the panels) for all the Rayleigh numbers. However, all the profiles agree well with those computed from (5.6) (orange dashed curves) with the coefficients provided in table 2.

Run	Ra	a	b	c	a_S
1	5×10^5	0.92	3.77	9.47	0.94
2	10^6	1.32	2.75	2.64	1.58
3	10^7	1.47	3.06	2.41	2.16
4	10^8	1.42	3.29	2.86	2.43
5	10^9	1.79	3.85	2.22	3.07

TABLE 2. The coefficients a, b, c are obtained by fitting the horizontally- and temporally-averaged profiles with (5.6). These coefficients are used to compute the profiles exhibited as orange dashed curves in figure 15. The coefficient a_S is obtained by fitting $|\kappa_{turb}/\kappa| = a_S^3 \xi^3$ in the region $\xi = 0$ to 0.05; it differs from the coefficient a.

decreases according to a power law, except for the data point at $Ra = 5 \times 10^5$, which does not seem to follow the scaling very well. Weaker temperature fluctuations due to smaller Ra might be the reason for this discrepancy. The best fit for $Ra \geq 10^6$ yields $\delta_\sigma/H = (2.3 \pm 0.1)Ra^{-0.25 \pm 0.005}$, which is close to the scaling of $\delta_{\langle T \rangle}$ (shown as a black dashed line in figure 14a). The maximum amplitude of the temperature fluctuations is plotted as a function of Ra in figure 14(b), which again shows that the data point at the lowest Ra does not follow the trend for higher Ra. The best fit for $Ra \geq 10^6$ yields $(\sigma_T)_{max}/\Delta T = (0.19 \pm 0.003)Ra^{-0.02 \pm 0.002}$. Thus, $(\sigma_T)_{max}/\Delta T$ decreases very weakly with increasing Ra in our 2-D RBC.

Note that $(\sigma_T)_{max}$ indicates the disparity between the temperatures of the ambient fluid and the plumes at the edge of the thermal BL. It is observed in RBC that the approach of the horizontally- and temporally-averaged profile towards the bulk temperature becomes slower with increasing Ra (see figure 15 for the mean thermal BL profiles in our flow) (Scheel & Schumacher 2016; Shishkina *et al.* 2017). Therefore, with increasing Ra, the temperature of the ambient fluid at the edge of the thermal BL becomes slightly closer to the temperature at the plate, which means that the contrast between the temperatures of the plumes and the ambient fluid at the BL height decreases, as the temperature of

the plumes remains nearly the same within the BL. This decreasing disparity at the edge of the BL with increasing Ra yields a decreasing $(\sigma_T)_{max}$ in figure 14(b). Moreover, we find that $(\sigma_T)_{max}/\Delta T \approx 0.14$ for $Ra = 10^7$ in our 2-D RBC, which is larger than the value $(\sigma_T)_{max}/\Delta T \approx 0.11$ observed by Scheel & Schumacher (2016) for $Pr = 0.021$, $Ra = 10^7$ in a cylindrical cell of aspect ratio one. This difference can be explained by the observation of van der Poel *et al.* (2013), who noted that the thermal BL profile in 2-D RBC is closer to the PBP profile than that in 3-D RBC for similar parameters. We also observe this when we compare the mean thermal BL profile for $Ra = 10^7$ in our flow (see figure 15) with the corresponding profile in figure 8 of Scheel & Schumacher (2016). Thus, the aforementioned temperature disparity at the edge of the thermal BL is smaller in 3-D RBC, which results in a smaller $(\sigma_T)_{max}$ in 3-D than in 2-D RBC. A weakly decreasing $(\sigma_T)_{max}$ in our 2-D RBC indicates that the aforementioned temperature disparity at the thermal BL height decreases slowly, or, in other words, the deviation of mean thermal BL profile from the PBP profile increases slowly in 2-D RBC with increasing Ra.

5. Thermal boundary layer profiles

We compare the temperature profiles in the BL region with the PBP profile, which is obtained by solving the following equations (Shishkina *et al.* 2010; Scheel *et al.* 2012):

$$\frac{d^3\Psi}{d\xi^3} + \frac{1}{2}\Psi\frac{d^2\Psi}{d\xi^2} = 0, \tag{5.1}$$

$$\frac{d^2\Theta}{d\xi^2} + \frac{1}{2}Pr\Psi\frac{d\Theta}{d\xi} = 0, \tag{5.2}$$

with the boundary conditions

$$\Psi(0) = 0, \quad \frac{d\Psi}{d\xi}(0) = 0, \quad \frac{d\Psi}{d\xi}(\infty) = 1, \tag{5.3a–c}$$

$$\Theta(0) = 0, \quad \Theta(\infty) = 1. \tag{5.4a,b}$$

Here, Ψ is the stream function, whose derivative yields the horizontal velocity (i.e. $u_x = d\Psi/d\xi$), and Θ is the normalized temperature, defined as

$$\Theta = \frac{T_{bot} - T}{T_{bot} - T_\infty}, \tag{5.5}$$

where $T_{bot} = 1$ is the temperature at the bottom plate and T_∞ is the temperature in the bulk region. The similarity variable ξ is defined as z/l, with l being the characteristic length scale of the thermal BL, which is $\delta_{(T)}$ in the present case. We solve (5.1) and (5.2) together with the prescribed boundary conditions (5.3a–c) and (5.4a,b) using the shooting method to obtain Θ and Ψ as a function of ξ.

We compare the temperature profiles measured at various horizontal positions at the plate with the PBP profile. However, we first compare the horizontally- and temporally-averaged profiles, as they have been observed to show stronger deviations from the PBP profile (Shishkina & Thess 2009).

5.1. *Mean boundary layer profiles*

To compare our temperature profiles with the PBP profile, we transform $T(z)$ near the bottom plate to obtain Θ by using $T_\infty = T_{bulk} = 0.5$ in (5.5). We similarly transform $T(z)$

near the top plate as $\Theta = (T - T_{top})/(T_\infty - T_{top})$, where $T_{top} = 0$ is the temperature at the top plate. We compare the horizontally- and temporally-averaged profiles $\langle T \rangle_{x,t}$ near the plate by plotting Θ obtained by using $T = \langle T \rangle_{x,t}$ in (5.5) and in the aforementioned relation for Θ near the top plate as a function of $\xi = z/\delta_{\langle T \rangle}$ in figure 15. We further average over the top and bottom halves of the domain due to the top-bottom symmetry of our flow. We observe that the profiles for all the Rayleigh numbers deviate from the PBP profile, and the deviation increases with increasing Ra. Moreover, the approach to the bulk temperature becomes slower as Ra increases. The reason for the deviation is that the RBC flow in a bounded domain does not satisfy the criteria for the PBP profile due to the presence of other effects, such as the emission of thermal plumes, buoyancy, pressure gradient, turbulent fluctuations, sidewalls, etc. Therefore, modified BL profiles in RBC have been suggested by incorporating these additional effects in the laminar BL equations (Shi *et al.* 2012; Shishkina *et al.* 2015; Ovsyannikov *et al.* 2016; Shishkina *et al.* 2017; Ching *et al.* 2019). Shishkina *et al.* (2017) and Ching *et al.* (2019) recently proposed a model of the horizontally- and temporally-averaged temperature profiles in the BL region by incorporating the effects of turbulent fluctuations in the laminar BL equations. They proposed that the temperature profile could be fitted with an equation of the form

$$\Theta(\xi) = \frac{1}{b} \int_0^{b\xi} \left[1 + \frac{3a^3}{b^3} (\eta - \arctan(\eta)) \right]^{-c} d\eta, \tag{5.6}$$

where the coefficients a, b, c can be obtained by fitting the temperature profile with this equation. The equation (5.6) was obtained by considering the variation of the turbulent diffusivity κ_{turb} near the plate. Shishkina *et al.* (2015) observed that $|\kappa_{turb}/\kappa|$ can be approximated as $a_S^3 \xi^3$ in the vicinity of the bottom plate, and as ξ in the logarithmic region far away from the plate.

Using our DNS data, we compute the turbulent diffusivity, defined as

$$\kappa_{turb}(\boldsymbol{x}) = -\frac{\langle u_z' T' \rangle_t}{\partial \langle T \rangle_t / \partial z}, \tag{5.7}$$

where u_z' and T' are the fluctuations in the vertical velocity and the temperature, respectively, from the time-averaged fields, and are defined as follows:

$$u_z(\boldsymbol{x}, t) = \langle u_z \rangle_t(\boldsymbol{x}) + u_z'(\boldsymbol{x}, t), \tag{5.8}$$

$$T(\boldsymbol{x}, t) = \langle T \rangle_t(\boldsymbol{x}) + T'(\boldsymbol{x}, t). \tag{5.9}$$

We plot the horizontally-averaged $|\kappa_{turb}/\kappa|$ normalized by ξ^3 in figure 16(*a*) and observe that κ_{turb} indeed scales as ξ^3 near the plate for all the Rayleigh numbers. However, the ξ^3 scaling is satisfied only up to $\xi \approx 0.05$, beyond which the scaling exponent decreases for all Ra. We obtain a_S for all the Rayleigh numbers by fitting $|\kappa_{turb}/\kappa| = a_S^3 \xi^3$ up to $\xi = 0.05$ (Shishkina *et al.* 2015). Figure 16(*a*) also shows that the prefactor a_S, which is a measure of the strength of turbulent fluctuations, increases with increasing Ra. We fit the temperature profiles shown in figure 15 with (5.6) and obtain the coefficients a, b, c. We then compute the theoretical profiles using (5.6) with the obtained coefficients a, b, c, and display them in figure 15. The figure shows that the temperature profiles obtained from our 2-D DNS can be described well by (5.6) with the proper choice of the coefficients a, b, c, which are summarized in table 2.
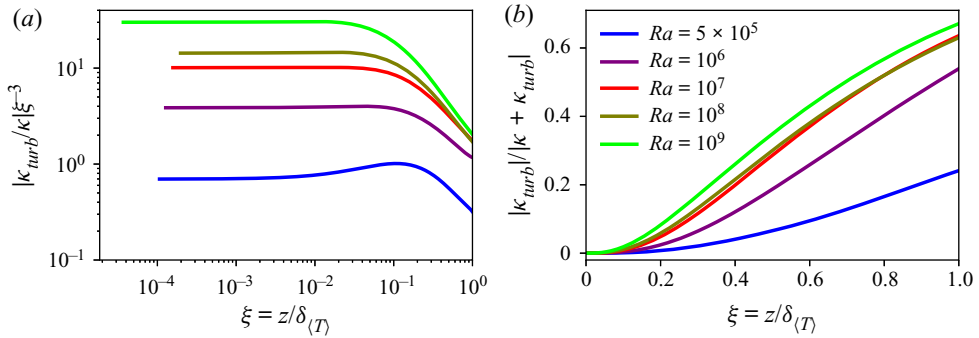
FIGURE 16. (*a*) Vertical profiles of the horizontally-averaged turbulent diffusivity $|\kappa_{turb}/\kappa|$ vary as ξ^3 in the vicinity of the bottom plate for all *Ra*, which is consistent with observations in 3-D RBC for different Prandtl numbers (Shishkina *et al.* 2015; Wang *et al.* 2018). (*b*) Variation of $|\kappa_{turb}|/|\kappa + \kappa_{turb}|$, signifying the fraction of heat transport due to turbulent fluctuations, indicates that the turbulent heat flux becomes increasingly important within the BL region with increasing *Ra*.

5.2. *Local boundary layer profiles*

We now compare the local BL profiles in the ejection, impact and shear regions with the PBP profile. To do this, we compute the time-averaged profiles $\langle T(x_0) \rangle_t$ at $x_0 = L/4, L/2, 3L/4$ and transform them using (5.5) to get the normalized temperature profile $\Theta(\xi)$. In figure 17, we plot the scaled temperature $\Theta_s = \Theta(\xi)/\Theta(\xi = 3)$ as a function of $\xi = z/\delta_{\langle T \rangle}(x_0)$; i.e. ξ is defined using the local BL thickness. We use this additional normalization because Θ does not saturate to unity in many of our profiles, and therefore, it may be normalized with a value of Θ in the region far from the BL, such as with $\Theta(\xi = 3)$ (Zhou *et al.* 2011; Stevens *et al.* 2012).

Figure 17 shows that the scaled BL profiles $\Theta_s(\xi)$ agree with the PBP profile only in a region very close to the bottom plate, i.e. up to $\xi \approx 1/2$. For $Ra = 10^6$ (figure 17*a*), the profiles in the impact and ejection regions deviate from the PBP profile for $\xi \geqslant 0.5$. However, $\Theta_s(\xi)$ in the shear region agrees with the PBP profile relatively well over the entire range of ξ. Moreover, $\Theta_s(\xi)$ in the ejection region for $Ra = 10^6$ exhibits overshoot, which is due to the growth of the corner roll in the impact region on the same plate. The overshoot in a profile indicates that the local temperature gradient is larger than that of the PBP profile. To investigate the reason for this overshoot, we look at the instantaneous normalized profiles in the ejection region and find that not all the profiles exhibit overshoot. We observe that just before the occurrence of the overshoot the size of the corner roll in the impact region, i.e. near the opposite sidewall, grows. As a result, the impinging plumes are diverted towards the ejection region. This causes an increase of the local temperature gradient in the ejection region, which is reflected as overshoot in the corresponding instantaneous temperature profile. As the flow evolution is nearly periodic for $Ra = 10^6$ (see figure 5*b* and supplementary movies), the aforementioned growth of the corner vortices occurs regularly, and thus, the overshoot is also present in the time-averaged profile. We do not observe the overshoot in the profiles for $Ra \geq 10^7$, as the corner flow structures become weaker for $Ra > 10^6$ in our low-*Pr* RBC. For $Ra \geq 10^7$, we find that $\Theta_s(\xi)$ deviates from the PBP profile in all three regions. Additionally, the values of $\Theta_s(\xi)$ in the shear and impact regions agree well with each other for the almost entire
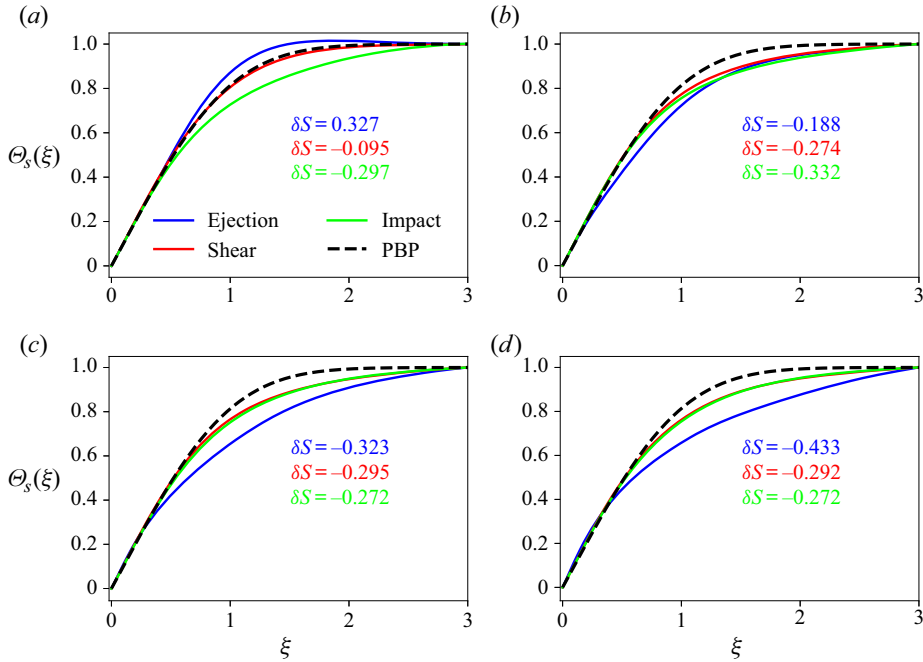
FIGURE 17. BL profiles of the scaled temperature $\Theta_s = \Theta(\xi)/\Theta(\xi = 3)$ in the ejection, shear and impact regions for (a) $Ra = 10^6$, (b) $Ra = 10^7$, (c) $Ra = 10^8$ and (d) $Ra = 10^9$. Deviation from the PBP profile (indicated as a black dashed curve in each panel) can be observed in nearly all the profiles. The deviation δS of the shape factor of each profile from that of the PBP profile is also indicated with the corresponding colour.

range of ξ for $Ra \geq 10^7$, which is consistent with the observation from figure 7. We find that the profiles measured in the ejection region deviate most from the PBP profile.

The quality of agreement of the BL profiles with the PBP profile can be quantified by computing the shape factor of the profiles (Schlichting & Gersten 2004), which is defined as

$$S = \delta_d/\delta_m, \tag{5.10}$$

where δ_d and δ_m are respectively the displacement and the momentum thicknesses of the profiles, and are computed as

$$\delta_d = \int_0^\infty \left(1 - \frac{\Theta(\xi)}{[\Theta(\xi)]_{max}}\right) d\xi, \tag{5.11}$$

$$\delta_m = \int_0^\infty \left(1 - \frac{\Theta(\xi)}{[\Theta(\xi)]_{max}}\right)\left(\frac{\Theta(\xi)}{[\Theta(\xi)]_{max}}\right) d\xi. \tag{5.12}$$

The shape factor of the PBP profile depends on the Prandtl number, and for $Pr = 0.021$ the shape factor is $S_{PBP} = 2.47$. Note that the shape factor of a profile indicates its tendency to quickly approach its asymptotic value; the larger the shape factor the faster the profile approaches its asymptotic value, and vice versa (Zhou *et al.* 2010; Scheel *et al.* 2012). We compute the shape factors of the profiles shown in figure 17 and indicate the deviation $\delta S = S - S_{PBP}$ from the shape factor of the PBP profile with the corresponding colours in the same figure. Note however that, to compute δ_d and δ_m of the profiles, we perform

integration only up to $\xi = 3$. We observe that δS is negative for most of the profiles in figure 17, except for $\Theta_s(\xi)$ in the ejection region for $Ra = 10^6$, which exhibits the overshoot. We can see from figure 17 that the values of δS for the profiles in the shear and impact regions do not differ much for $Ra \geq 10^7$, thus quantitatively indicating their similarity.

Zhou & Xia (2010) observed that the BL profiles of the horizontal velocity in a high-Pr RBC (water) agree better with the Prandtl–Blasius velocity profile if they are measured in a time-dependent frame of reference relative to the instantaneous BL width and then averaged in time. This dynamic rescaling was also applied to the thermal BL profiles for moderate and high Prandtl numbers, and it was observed that the agreement of the rescaled profiles with the PBP profile becomes better (Zhou *et al.* 2010, 2011; Scheel *et al.* 2012; Shi *et al.* 2012; Stevens *et al.* 2012). Zhou *et al.* (2011) studied the structure of the BLs in a 2-D square box for $Pr = 4.4$ and $Ra = 10^8$ and found that the dynamically rescaled thermal BL profiles at nearly all the horizontal locations agree better with the PBP profile than do the corresponding unscaled profiles. Here, we want to test whether this rescaling works for thermal BL profiles in a low-Pr convection.

We thus construct a dynamically varying frame of reference as

$$\xi^*(t) = z/\delta_T(x_0, t), \tag{5.13}$$

and average the temperature profiles in this varying frame of reference as

$$\Theta^*(\xi^*) = \langle \Theta(t, z \,|\, z = \xi^*(t)\delta_T(x_0, t)\rangle_t. \tag{5.14}$$

This enables us to average the temperature field at the same relative distances compared to the instantaneous BL thicknesses, which fluctuate strongly in our low-Pr convection. We again compute the scaled profiles, defined as $\Theta_s^*(\xi^*) = \Theta^*(\xi^*)/\Theta^*(\xi^* = 3)$, and exhibit them in figure 18, which reveals that the dynamically rescaled profiles in the shear and impact regions agree very well with the PBP profile for all the Rayleigh numbers. The profiles in the ejection region, however, deviate even after the dynamic rescaling is applied, except for $Ra = 10^7$, where the agreement is rather good.

We again compute the deviation $\delta S^* = S^* - S_{PBP}$ for the rescaled profiles and indicate them in figure 18. We find for all the profiles that $|\delta S^*| < |\delta S|$, thus indicating that the agreement with the PBP profile becomes better if the profiles are measured in the dynamically rescaled frame (Zhou & Xia 2010). Furthermore, $|\delta S^*|$ for the profiles in the ejection region increases with increasing Ra, which indicates that the deviations in the thermal BL profiles in this region become stronger as Ra increases. Like the values of δS, the values of δS^* for the profiles in the shear and impact regions are very similar (and closer to zero) for all the Rayleigh numbers.

5.3. *Turbulent or not?*

We have observed in figure 7 that the profiles in the ejection region approach the bulk temperature slowly compared to those in the shear and impact regions. On the one hand, the rescaled profiles in the shear and impact regions are very similar to the PBP profile, which indicates that the fraction of the BL corresponding to these regions is laminar in the scalingwise sense. On the other hand, the profiles in the ejection region deviate conspicuously from the PBP profile, which implies that the local thermal BL properties in the ejection region differ from those of a laminar BL. Note that the shape factor of a turbulent BL profile is 1.28, which is smaller than S_{PBP} for $Pr = 0.021$. Thus, the
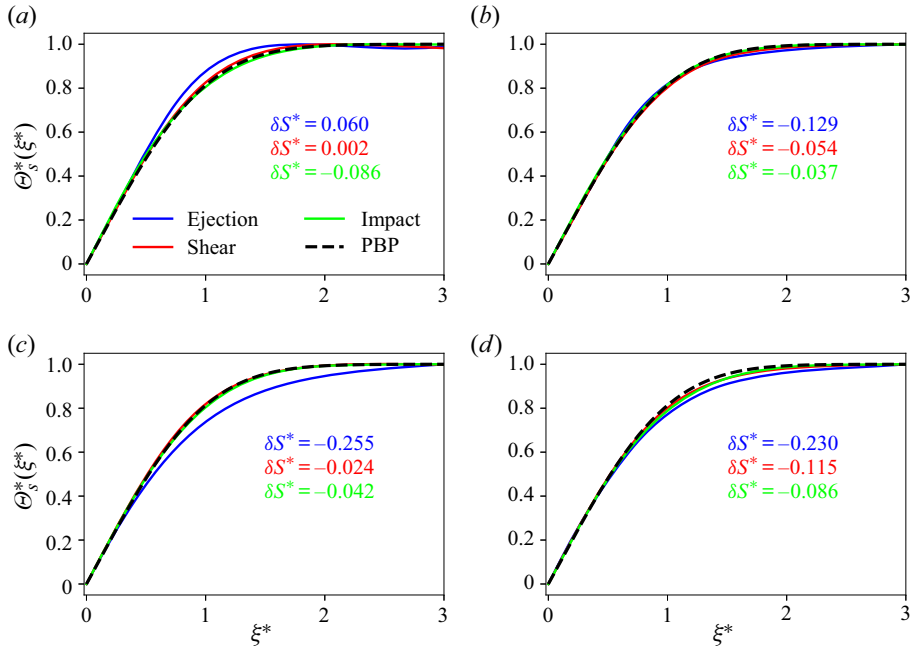
FIGURE 18. Dynamically rescaled thermal BL profiles for (*a*) $Ra = 10^6$, (*b*) $Ra = 10^7$, (*c*) $Ra = 10^8$ and (*d*) $Ra = 10^9$. The rescaled profiles in the shear and impact regions agree well with the PBP profile (black dashed curve), whereas those in the ejection regions deviate from it. The deviation of the shape factor δS^* for each profile is indicated with the corresponding colour.

increasing negative deviation in the shape factors of our profiles in the ejection region, which does not vanish even after the application of the dynamic rescaling, indicates that the ejection region becomes increasingly turbulent with increasing Ra. As the turbulent BL profiles exhibit a logarithmic scaling (Ahlers, Bodenschatz & He 2014; van der Poel *et al.* 2015; Schumacher *et al.* 2016; Zhu *et al.* 2018), we plot the local profiles near the bottom plate on a semilogarithmic scale to explore the logarithmic behaviour of our profiles. Time-averaged profiles in the ejection region, i.e. at $x_0 = L/4$, are exhibited in figure 19(*a*), where we observe in the profile for $Ra = 10^9$ that there exists a region between $z \approx 0.01$ and $z \approx 0.07$ which can be fitted as $\langle T(x_0, z)\rangle_t = A \log(z) + B$. The best fit yields $A = -0.30 \pm 0.001$ and $B = 0.23 \pm 0.001$; the resulting best fit curve is shown as an orange dashed curve in figure 19(*a*). Figure 19(*b*) shows the profiles in the impact region, i.e. at $x_0 = 3L/4$. We do not show the profiles in the shear region as they are very similar to the profiles in the impact region (see figure 7).

Figure 19 reveals that the other profiles do not exhibit a discernible logarithmic region as the profile in the ejection region for $Ra = 10^9$ does. The logarithmic behaviour of the profiles can be detected more clearly by looking at a diagnostic function $D(z) = dT/d \log z$, which should exhibit a plateau in the region where the temperature profile exhibits a logarithmic scaling (Shishkina & Thess 2009; Wagner *et al.* 2012; Zhou & Xia 2013; van der Poel *et al.* 2015). The insets of figure 19 show the diagnostic function $D(x_0, z) = \mathrm{d}\langle T(x_0)\rangle_t / \mathrm{d} \log z$ for the corresponding profiles, where we can see that no clear plateau can be observed in $D(x_0, z)$, except for $Ra = 10^9$ in the ejection region, where a plateau region exists for $\delta_{\langle T\rangle} \lesssim z \lesssim 3\delta_{\langle T\rangle}$. This range roughly corresponds to the observed
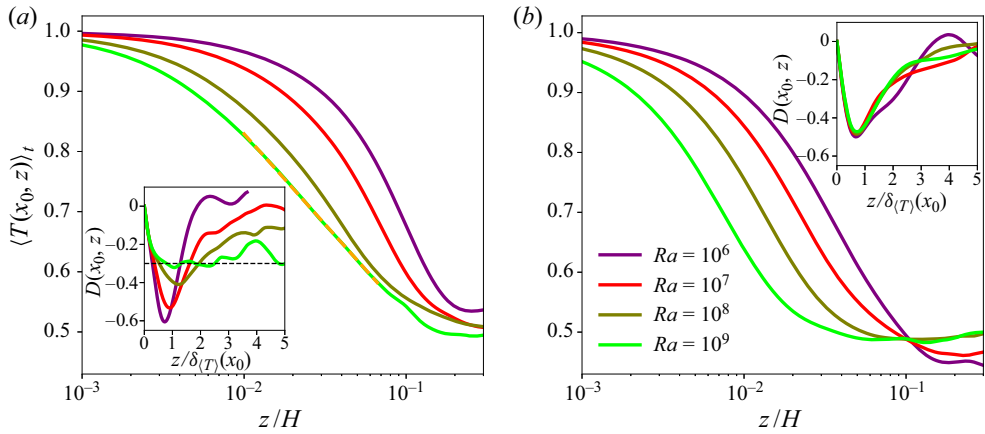
FIGURE 19. Time-averaged temperature profiles in (*a*) the ejection region at $x_0 = L/4$ and (*b*) the impact region at $x_0 = 3L/4$ on a semilogarithmic scale. The profile for $Ra = 10^9$ in (*a*) exhibits a discernible logarithmic region, and the resulting best fit curve is indicated as an orange dashed curve. Insets show the diagnostic function for the corresponding profiles as a function of the normalized vertical distance from the plate. A plateau region in $D(x_0, z)$ in (*a*) for $Ra = 10^9$ can be observed for $\delta_{\langle T \rangle} \lesssim z \lesssim 3\delta_{\langle T \rangle}$.

logarithmic range in the corresponding profile. We observe that $D(x_0, z)$ in figure 19(*a*) in the region $\delta_{\langle T \rangle} \lesssim z \lesssim 3\delta_{\langle T \rangle}$ is not a constant but fluctuates weakly around a mean value, which is due to a limited statistics available for this simulation. A longer simulation, and thus, a longer averaging would reduce the observed fluctuations in the plateau region.

Our observation that the temperature profile for $Ra = 10^9$ in the ejection region shows a discernible logarithmic range is similar to the observations of van der Poel *et al.* (2015), who observed logarithmic temperature profiles in the ejection region in 2-D RBC for $Pr = 1$, $Ra = 5 \times 10^{10}$. However, the slope $|A|$ of our profile is much larger than the slope of the logarithmic temperature profile in the bulk region observed by Ahlers *et al.* (2014) and van der Poel *et al.* (2015). Moreover, the logarithmic region observed here overlaps with the buffer layer and differs from the logarithmic temperature profile in the bulk of the domain (Ahlers *et al.* 2014; van der Poel *et al.* 2015).

Turbulent fluctuations in the BL region become stronger with increasing Ra, and fully turbulent BLs would prevail for sufficiently strong thermal forcing (Grossmann & Lohse 2000; Scheel & Schumacher 2017). However, for moderately strong thermal forcing the BLs are transitional: a fraction of them is turbulent, and the turbulent fraction grows continuously with increasing Ra (Scheel & Schumacher 2016; Schumacher *et al.* 2016). The strength of turbulent fluctuations within the BL region can be investigated by looking at the turbulent fraction of the total heat flux, which we compute as follows (Wagner *et al.* 2012):

$$F_{turb}(\boldsymbol{x}) = \frac{\langle u_z' T' \rangle_t(\boldsymbol{x})}{-\kappa \dfrac{\partial \langle T \rangle_t}{\partial z}(\boldsymbol{x}) + \langle u_z' T' \rangle_t(\boldsymbol{x})} = \frac{\kappa_{turb}(\boldsymbol{x})}{\kappa + \kappa_{turb}(\boldsymbol{x})}. \quad (5.15)$$

We plot the horizontally-averaged turbulent fraction $F_{turb}(z) = |\kappa_{turb}(z)|/|\kappa + \kappa_{turb}(z)|$ for all the Rayleigh numbers in figure 16(*b*), which reveals that $F_{turb}(0) = 0$, as the heat flux is purely diffusive at the horizontal plates. As one moves from the plate towards the bulk region, turbulent fluctuations start to contribute to the total heat transport, and
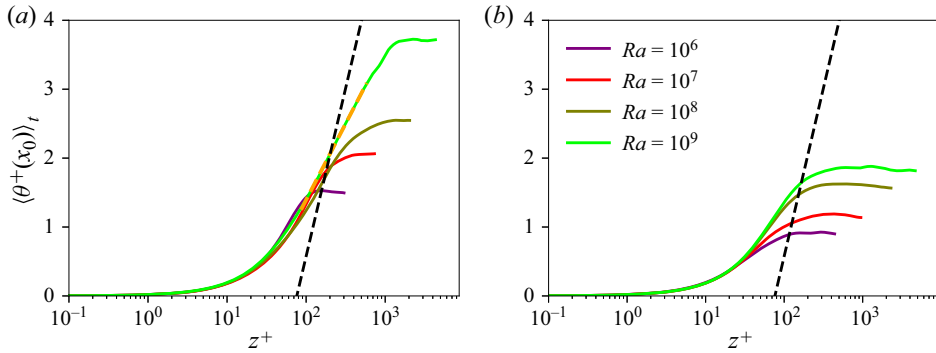
FIGURE 20. Time-averaged temperature profiles in the inner wall units measured in (*a*) the ejection region at $x_0 = L/4$ and (*b*) the impact region at $x_0 = 3L/4$. As in figure 19(*a*), the profile for $Ra = 10^9$ in panel (*a*) exhibits a logarithmic scaling for $85 \leq z^+ \leq 580$ with a slope $\alpha_f \approx 0.96$, which is less than that of a fully turbulent BL (shown as a black dashed line in both the panels). This indicates that the BLs in our low-*Pr* convection flow are not yet fully turbulent.

their contribution increases with increasing distance from the plate. Moreover, at the same relative distance from the plate, $F_{turb}(z)$ increases with increasing Ra. We observe that near $z \approx \delta_{\langle T \rangle}$ more than 50 % of heat is transported due to turbulent fluctuations for $Ra \geq 10^6$. Thus, the turbulent fluctuations are not negligible in the BL region in our low-*Pr* RBC.

Finally, we compare the local temperature profiles in our low-*Pr* RBC with the fully turbulent thermal BL profile, which exhibits a logarithmic region in the overlap layer (Yaglom 1979). To do this, we plot the profiles in inner wall units (Schumacher *et al.* 2016; Scheel & Schumacher 2017) by computing the local dimensionless friction velocity and friction temperature as

$$u_\tau(x_0) = \left(\frac{Pr}{Ra}\right)^{1/4} \left\langle \left[\left(\frac{\partial u_x}{\partial z}\right)^2 \Big|_{x_0, z=0} \right]^{1/4} \right\rangle_t, \tag{5.16}$$

$$T_\tau(x_0) = \left\langle \frac{1}{u_\tau(x_0, t)\sqrt{RaPr}} \frac{\partial T}{\partial z}\Big|_{x_0, z=0} \right\rangle_t, \tag{5.17}$$

where the derivatives at x_0 in the above equations are averaged in the region $x_0 - 0.02L \leq x \leq x_0 + 0.02L$, with $x_0 = L/4, L/2, 3L/4$. The resulting local viscous length scale of the BL is given by

$$z_\tau(x_0) = \sqrt{\frac{Pr}{Ra}} \frac{1}{u_\tau(x_0)}. \tag{5.18}$$

To compare our profiles in the inner wall units, we define a temperature θ as

$$\theta(z) = (T_{bot} - T(z))/\Delta T \tag{5.19}$$

and plot the rescaled temperature $\langle \theta^+(x_0, z) \rangle_t = \langle \theta(x_0, z) \rangle_t / T_\tau(x_0)$ as a function of $z^+ = z/z_\tau(x_0)$ in figure 20. The rescaled profiles in the ejection region are exhibited in figure 20(*a*), where we observe that the profiles become more log-like with increasing Ra, and for $Ra = 10^9$, $\langle \theta^+(x_0, z) \rangle_t$ exhibits a discernible logarithmic scaling in some range

of z^+. Following Yaglom ([1979](#)) and Kader ([1981](#)), the logarithmic temperature profile in the fully turbulent BL should scale as

$$\langle \theta^+(z) \rangle = \alpha \ln z^+ + \beta(Pr), \tag{5.20}$$

with $\alpha = 2.12$ and

$$\beta(Pr) = (3.8Pr^{1/3} - 1)^2 - 1 + 2.12 \ln Pr. \tag{5.21}$$

We fit the profile for $Ra = 10^9$ in the ejection region with (5.20) for z^+ in the range 85–580, which corresponds to the fitting range shown in [figure 19](#)(*a*). The best fit yields a slope $\alpha_f = 0.96 \pm 0.001$, which is less than $\alpha = 2.12$ for the fully turbulent thermal BL. As is evident from [figure 20](#), the other profiles do not exhibit a clear logarithmic region; therefore we do not fit them with (5.20). Thus, our results indicate that the BLs in our 2-D RBC for $Pr = 0.021$ are transitional and the highest Ra achieved in this work is still not enough to yield a fully turbulent thermal BL.

6. Conclusions

In this paper, we explored the structure of the thermal BL in low-Pr RBC in a 2-D square box by performing DNS for $Pr = 0.021$ and Rayleigh numbers up to 10^9, which has never been achieved before. Interestingly, we found that the Nusselt numbers in our simulations agree reasonably well with those obtained by Scheel & Schumacher ([2017](#)) for $Pr = 0.021$ in a cylindrical cell. This similarity in Nu implies that the scaling of the local thermal BL thickness observed in our 2-D RBC, as well as its horizontal structure, might also be similar in 3-D convection for low Prandtl numbers. The LSC yields three distinct flow regions at the horizontal plates, and we found that the properties of the thermal BL are different in these regions. The temperature profiles measured in the plume-ejection region approach the bulk temperature slowly compared to the profiles in the shear and impact regions. We observed that the thermal BL profiles in all regions deviate from the PBP profile, and the strongest deviations are found in the ejection region. This is because the turbulent fluctuations are stronger in the ejection region, and therefore, the local BL properties in this region deviate the most from the properties of a laminar BL. The dynamically rescaled profiles (Zhou & Xia [2010](#)) in the shear and impact regions agree well with the PBP profile for all the Rayleigh numbers, suggesting that these regions in the BL are laminar in the scalingwise sense. The rescaled profiles in the ejection region, however, exhibit persistent deviations (Shi *et al.* [2012](#)) for all the Rayleigh numbers in our study. By comparing our profiles with the turbulent BL profile, we concluded that the thermal BLs in our low-Pr convection are transitional and become increasingly turbulent with increasing Ra (Schumacher *et al.* [2016](#)).

The horizontal structure of the thermal BL in low-Pr convection has not previously been investigated, and therefore, to do this, we computed the time-averaged local BL thicknesses $\delta_{\langle T \rangle}(x)$ at the top and bottom plates. Our findings revealed that the $\delta_{\langle T \rangle}(x)$ are larger in the ejection region and decrease as the impact region is approached. Thus, the local thermal BL thickness in our 2-D RBC grows in the downstream direction. However, $\delta_{\langle T \rangle}(x)$ in our flow grows neither as $\sqrt{x}$ as in a laminar BL nor as x as in a turbulent BL (Schlichting & Gersten [2004](#)). We moreover found that $\delta_{\langle T \rangle}(x)$ at every horizontal location decreases as $Ra^{-\beta(x)}$, with the exponent $\beta(x)$ depending on the position at the plates. We found that the local exponents $\beta(x)$ in the ejection region are larger than those in the impact and shear regions. As $\delta_{\langle T \rangle}(x)$ is inversely proportional to the diffusive heat flux at the plate, we found that the local diffusive heat flux at the plate is smaller in the ejection region than in

the shear and impact regions. Moreover, the diffusive flux at the plate generally increases in the ejection region but decreases in the other two regions with increasing Ra, which implies that the local BL thicknesses scale differently with Ra compared to the scaling of mean BL thickness. A position-dependent exponent $\beta(x)$ implies that the horizontal variation of the BL thickness becomes weaker with increasing Ra, which is due to the growing strength of LSC with increasing Ra in our flow. We estimated that $\delta_{\langle T \rangle}(x)$ might be the same throughout the plate for $Ra \geq 8 \times 10^{12}$ in our low-Pr convection, provided that the observed scalings of the local BL thicknesses hold also for the larger Ra.

Our observation of the position-dependent properties of the temperature field near the isothermal plates in low-Pr convection is consistent with a similar picture found in high- and moderate-Pr convection (van der Poel *et al.* 2015; Zhu *et al.* 2018; He & Xia 2019). However, as the temporal evolution of the thermal BL is correlated with that of the viscous BL (Zhou *et al.* 2010; Shi *et al.* 2012), for improved understanding it is crucial to study the properties of viscous BLs in our low-Pr RBC. This is currently underway and will be reported elsewhere.

Acknowledgements

Declaration of interests

The author reports no conflict of interest.

Supplementary movies

Supplementary movies are available at https://doi.org/10.1017/jfm.2020.961.

REFERENCES

AHLERS, G., BODENSCHATZ, E. & HE, X. 2014 Logarithmic temperature profiles of turbulent Rayleigh–Bénard convection in the classical and ultimate state for a Prandtl number of 0.8. *J. Fluid Mech.* **758**, 436–467.

AHLERS, G., GROSSMANN, S. & LOHSE, D. 2009 Heat transfer and large scale dynamics in turbulent Rayleigh–Bénard convection. *Rev. Mod. Phys.* **81**, 503–537.

BHATTACHARYA, S., SAMTANEY, R. & VERMA, M. K. 2019 Scaling and spatial intermittency of thermal dissipation in turbulent convection. *Phys. Fluids* **31** (7), 075104.

CHANDRA, M. & VERMA, M. K. 2013 Flow reversals in turbulent convection via vortex reconnections. *Phys. Rev. Lett.* **110**, 114503.

CHANDRASEKHAR, S. 1981 *Hydrodynamic and Hydromagnetic Stability*. Dover.

CHEN, X., HUANG, S.-D., XIA, K.-Q. & XI, H.-D. 2019 Emergence of substructures inside the large-scale circulation induces transition in flow reversals in turbulent thermal convection. *J. Fluid Mech.* **877**, R1.

CHILLÀ, F. & SCHUMACHER, J. 2012 New perspectives in turbulent Rayleigh–Bénard convection. *Eur. Phys. J.* E **35**, 58.

CHING, E. S. C., LEUNG, H. S., ZWIRNER, L. & SHISHKINA, O. 2019 Velocity and thermal boundary layer equations for turbulent Rayleigh–Bénard convection. *Phys. Rev. Res.* **1**, 033037.

CIONI, S., CILIBERTO, S. & SOMMERIA, J. 1997 Strongly turbulent Rayleigh–Bénard convection in mercury: comparison with results at moderate Prandtl number. *J. Fluid Mech.* **335**, 111–140.

DEARDORFF, J. W. & WILLIS, G. E. 1967 Investigation of turbulent thermal convection between horizontal plates. *J. Fluid Mech.* **28** (4), 675–704.

FISCHER, P. F. 1997 An overlapping Schwarz method for spectral element solution of the incompressible Navier–Stokes equations. *J. Comput. Phys.* **133** (1), 84–101.

GLAZIER, J., SEGAWA, T., NAERT, A. & SANO, M. 1999 Evidence against 'ultrahard' thermal turbulence at very high Rayleigh numbers. *Nature* **398**, 307–310.

GROSSMANN, S. & LOHSE, D. 2000 Scaling in thermal convection: a unifying theory. *J. Fluid Mech.* **407**, 27.

HANASOGE, S., GIZON, L. & SREENIVASAN, K. R. 2016 Seismic sounding of convection in the sun. *Annu. Rev. Fluid Mech.* **48**, 191–217.

HE, Y.-H. & XIA, K.-Q. 2019 Temperature fluctuation profiles in turbulent thermal convection: a logarithmic dependence versus a power-law dependence. *Phys. Rev. Lett.* **122**, 014503.

HORN, S., SHISHKINA, O. & WAGNER, C. 2013 On non-Oberbeck–Boussinesq effects in three-dimensional Rayleigh–Bénard convection in glycerol. *J. Fluid Mech.* **724**, 175–202.

KADER, B. 1981 Temperature and concentration profiles in fully turbulent boundary layers. *Intl J. Heat Mass Transfer* **24** (9), 1541–1544.

LANDAU, L. D. & LIFSHITZ, E. M. 1987 *Fluid Mechanics*. Pergamon.

LUI, S.-L. & XIA, K.-Q. 1998 Spatial structure of the thermal boundary layer in turbulent convection. *Phys. Rev.* E **57**, 5494–5503.

NIEMELA, J. J. & SREENIVASAN, K. R. 2003 Rayleigh–number evolution of large-scale coherent motion in turbulent convection. *Europhys. Lett.* **62**, 829–833.

OVSYANNIKOV, M., KRASNOV, D., EMRAN, M. S. & SCHUMACHER, J. 2016 Combined effects of prescribed pressure gradient and buoyancy in boundary layer of turbulent Rayleigh–Bénard convection. *Eur. J. Mech.* B/*Fluids* **57**, 64–74.

PANDEY, A., SCHEEL, J. D. & SCHUMACHER, J. 2018*a* Turbulent superstructures in Rayleigh–Bénard convection. *Nat. Commun.* **9**, 2118.

PANDEY, A. & VERMA, M. K. 2016 Scaling of large-scale quantities in Rayleigh–Bénard convection. *Phys. Fluids* **28**, 095105.

PANDEY, A., VERMA, M. K. & BARMA, M. 2018*b* Reversals in infinite-Prandtl-number Rayleigh–Bénard convection. *Phys. Rev.* E **98**, 023109.

PANDEY, A., VERMA, M. K., CHATTERJEE, A. G. & DUTTA, B. 2016 Similarities between 2-D and 3-D convection for large Prandtl number. *Pramana J. Phys.* **87**, 13.

PANDEY, A., VERMA, M. K. & MISHRA, P. K. 2014 Scaling of heat flux and energy spectrum for very large Prandtl number convection. *Phys. Rev.* E **89**, 023006.

PODVIN, B. & SERGENT, A. 2015 A large-scale investigation of wind reversal in a square Rayleigh–Bénard cell. *J. Fluid Mech.* **766**, 172–201.

VAN DER POEL, E. P., OSTILLA-MÓNICO, R., VERZICCO, R., GROSSMANN, S. & LOHSE, D. 2015 Logarithmic mean temperature profiles and their connection to plume emissions in turbulent Rayleigh–Bénard convection. *Phys. Rev. Lett.* **115**, 154501.

VAN DER POEL, E. P., STEVENS, R. J. A. M. & LOHSE, D. 2013 Comparison between two- and three-dimensional Rayleigh–Bénard convection. *J. Fluid Mech.* **736**, 177–194.

SCHEEL, J. D., EMRAN, M. S. & SCHUMACHER, J. 2013 Resolving the fine-scale structure in turbulent Rayleigh–Bénard convection. *New J. Phys.* **15**, 113063.

SCHEEL, J. D., KIM, E. & WHITE, K. R. 2012 Thermal and viscous boundary layers in turbulent Rayleigh–Bénard convection. *J. Fluid Mech.* **711**, 281–305.

SCHEEL, J. D. & SCHUMACHER, J. 2014 Local boundary layer scales in turbulent Rayleigh–Bénard convection. *J. Fluid Mech.* **758**, 344–373.

SCHEEL, J. D. & SCHUMACHER, J. 2016 Global and local statistics in turbulent convection at low Prandtl numbers. *J. Fluid Mech.* **802**, 147–173.

SCHEEL, J. D. & SCHUMACHER, J. 2017 Predicting transition ranges to fully turbulent viscous boundary layers in low Prandtl number convection flows. *Phys. Rev. Fluids* **2**, 123501.

SCHLICHTING, H. & GERSTEN, K. 2004 *Boundary Layer Theory*. Springer.

SCHMALZL, J., BREUER, M. & HANSEN, U. 2004 On the validity of two-dimensional numerical approaches to time-dependent thermal convection. *Europhys. Lett.* **67**, 390–396.

SCHUMACHER, J., BANDARU, V., PANDEY, A. & SCHEEL, J. D. 2016 Transitional boundary layers in low-Prandtl-number convection. *Phys. Rev. Fluids* **1**, 084402.

SCHUMACHER, J., GÖTZFRIED, P. & SCHEEL, J. D. 2015 Enhanced enstrophy generation for turbulent convection in low-Prandtl-number fluids. *Proc. Natl Acad. Sci. USA* **112**, 9530–9535.

SCHUMACHER, J. & SREENIVASAN, K. R. 2020 Colloquium: unusual dynamics of convection in the sun. *Rev. Mod. Phys.* **92**, 041001.

SHI, N., EMRAN, M. S. & SCHUMACHER, J. 2012 Boundary layer structure in turbulent Rayleigh–Bénard convection. *J. Fluid Mech.* **706**, 5–33.

SHISHKINA, O., HORN, S., EMRAN, M. S. & CHING, E. S. C. 2017 Mean temperature profiles in turbulent thermal convection. *Phys. Rev. Fluids* **2**, 113502.

SHISHKINA, O., HORN, S., WAGNER, S. & CHING, E. S. C. 2015 Thermal boundary layer equation for turbulent Rayleigh–Bénard convection. *Phys. Rev. Lett.* **114**, 114302.

SHISHKINA, O., STEVENS, R., GROSSMANN, S. & LOHSE, D. 2010 Boundary layer structure in turbulent thermal convection and its consequences for the required numerical resolution. *New J. Phys.* **12**, 075022.

SHISHKINA, O. & THESS, A. 2009 Mean temperature profiles in turbulent Rayleigh–Bénard convection of water. *J. Fluid Mech.* **633**, 449–460.

SHISHKINA, O. & WAGNER, C. 2008 Analysis of sheet-like thermal plumes in turbulent Rayleigh–Bénard convection. *J. Fluid Mech.* **599**, 383–404.

SHRAIMAN, B. I. & SIGGIA, E. D. 1990 Heat transport in high-Rayleigh–number convection. *Phys. Rev. A* **42**, 3650–3653.

SILANO, G., SREENIVASAN, K. R. & VERZICCO, R. 2010 Numerical simulations of Rayleigh–Bénard convection for Prandtl numbers between 10^{-1} and 10^4 and Rayleigh numbers between 10^5 and 10^9. *J. Fluid Mech.* **662**, 409–446.

STEVENS, R., LOHSE, D. & VERZICCO, R. 2011 Prandtl and Rayleigh number dependence of heat transport in high Rayleigh number thermal convection. *J. Fluid Mech.* **688**, 31–43.

STEVENS, R. J. A. M., ZHOU, Q., GROSSMANN, S., VERZICCO, R., XIA, K.-Q. & LOHSE, D. 2012 Thermal boundary layer profiles in turbulent Rayleigh–Bénard convection in a cylindrical sample. *Phys. Rev. E* **85**, 027301.

SUGIYAMA, K., NI, R., STEVENS, R. J. A. M., CHAN, T. S., ZHOU, S.-Q., XI, H.-D., SUN, C., GROSSMANN, S., XIA, K.-Q. & LOHSE, D. 2010 Flow reversals in thermally driven turbulence. *Phys. Rev. Lett.* **105**, 034503.

VERMA, M. K. 2018 *Physics of Buoyant Flows*. World Scientific.

VERMA, M. K., KUMAR, A. & PANDEY, A. 2017 Phenomenology of buoyancy-driven turbulence: recent results. *New J. Phys.* **19** (2), 025012.

WAGNER, S. & SHISHKINA, O. 2013 Aspect-ratio dependency of Rayleigh–Bénard convection in box-shaped containers. *Phys. Fluids* **25**, 085110.

WAGNER, S., SHISHKINA, O. & WAGNER, C. 2012 Boundary layers and wind in cylindrical Rayleigh–Bénard cells. *J. Fluid Mech.* **697**, 336–366.

WANG, J. & XIA, K.-Q. 2003 Spatial variations of the mean and statistical quantities in the thermal boundary layers of turbulent convection. *Eur. Phys. J. B* **32**, 127–136.

WANG, Y., HE, X. & TONG, P. 2016 Boundary layer fluctuations and their effects on mean and variance temperature profiles in turbulent Rayleigh–Bénard convection. *Phys. Rev. Fluids* **1**, 082301.

WANG, Y., XU, W., HE, X., YIK, H., WANG, X., SCHUMACHER, J. & TONG, P. 2018 Boundary layer fluctuations in turbulent Rayleigh–Bénard convection. *J. Fluid Mech.* **840**, 408–431.

WERNE, J. 1993 Structure of hard-turbulent convection in two dimensions: numerical evidence. *Phys. Rev. E* **48**, 1020–1035.

YAGLOM, A. M. 1979 Similarity laws for constant-pressure and pressure-gradient turbulent wall flows. *Annu. Rev. Fluid Mech.* **11** (1), 505–540.

ZHANG, S., XIA, Z., ZHOU, Q. & CHEN, S. 2020 Controlling flow reversal in two-dimensional Rayleigh–Bénard convection. *J. Fluid Mech.* **891**, R4.

ZHANG, Y., HUANG, Y.-X., JIANG, N., LIU, Y.-L., LU, Z.-M., QIU, X. & ZHOU, Q. 2017*a* Statistics of velocity and temperature fluctuations in two-dimensional Rayleigh–Bénard convection. *Phys. Rev. E* **96**, 023105.

ZHANG, Y., ZHOU, Q. & SUN, C. 2017*b* Statistics of kinetic and thermal energy dissipation rates in two-dimensional turbulent Rayleigh–Bénard convection. *J. Fluid Mech.* **814**, 165–184.

ZHOU, Q., STEVENS, R. J. A. M., SUGIYAMA, K., GROSSMANN, S., LOHSE, D. & XIA, K.-Q. 2010 Prandtl–Blasius temperature and velocity boundary-layer profiles in turbulent Rayleigh–Bénard convection. *J. Fluid Mech.* **664**, 297–312.

ZHOU, Q., SUGIYAMA, K., STEVENS, R. J. A. M., GROSSMANN, S., LOHSE, D. & XIA, K.-Q. 2011 Horizontal structures of velocity and temperature boundary layers in two-dimensional numerical turbulent Rayleigh–Bénard convection. *Phys. Fluids* **23** (12), 125104.

ZHOU, Q., SUN, C. & XIA, K.-Q. 2007 Morphological evolution of thermal plumes in turbulent Rayleigh–Bénard convection. *Phys. Rev. Lett.* **98**, 074501.

ZHOU, Q. & XIA, K. Q. 2010 Measured instantaneous viscous boundary layer in turbulent Rayleigh–Bénard convection. *Phys. Rev. Lett.* **104**, 104301.

ZHOU, Q. & XIA, K.-Q. 2013 Thermal boundary layer structure in turbulent Rayleigh–Bénard convection in a rectangular cell. *J. Fluid Mech.* **721**, 199–224.

ZHU, X., MATHAI, V., STEVENS, R. J. A. M., VERZICCO, R. & LOHSE, D. 2018 Transition to the ultimate regime in two-dimensional Rayleigh–Bénard convection. *Phys. Rev. Lett.* **120**, 144502.

ZÜRNER, T., SCHINDLER, F., VOGT, T., ECKERT, S. & SCHUMACHER, J. 2019 Combined measurement of velocity and temperature in liquid metal convection. *J. Fluid Mech.* **876**, 1108–1128.

ZWIRNER, L., KHALILOV, R., KOLESNICHENKO, I., MAMYKIN, A., MANDRYKIN, S., PAVLINOV, A., SHESTAKOV, A., TEIMURAZOV, A., FRICK, P. & SHISHKINA, O. 2020 The influence of the cell inclination on the heat transport and large-scale circulation in liquid metal convection. *J. Fluid Mech.* **884**, A18.